

Signatures of hypermassive neutron star lifetimes on r-process nucleosynthesis in the disk ejecta from neutron star mergers

Jonas Lippuner¹, Rodrigo Fernández^{2,3,4}, Luke F. Roberts^{5,6}, Francois Foucart^{7,8},
Daniel Kasen^{3,4,8}, Brian D. Metzger⁹, Christian D. Ott^{1,10}

¹ *TAPIR, Walter Burke Institute for Theoretical Physics, California Institute of Technology, Pasadena, CA 91125, USA*

² *Department of Physics, University of Alberta, Edmonton, AB T6G 2E1, Canada*

³ *Department of Physics, University of California, Berkeley, CA 94720, USA*

⁴ *Department of Astronomy & Theoretical Astrophysics Center, University of California, Berkeley, CA 94720, USA*

⁵ *National Superconducting Cyclotron Laboratory, Michigan State University, East Lansing, MI 48824, USA*

⁶ *Department of Physics and Astronomy, Michigan State University, East Lansing, MI 48824, USA*

⁷ *NASA Einstein Fellow*

⁸ *Nuclear Science Division, Lawrence Berkeley National Laboratory, Berkeley, CA 94720, USA*

⁹ *Columbia Astrophysics Laboratory, Columbia University, New York, NY 10027, USA*

¹⁰ *Center for Gravitational Physics and International Research Unit of Advanced Future Studies, Yukawa Institute for Theoretical Physics, Kyoto University, Kyoto, Kyoto Prefecture 606-8317, Japan*

Submitted to MNRAS

ABSTRACT

We investigate the nucleosynthesis of heavy elements in the winds ejected by accretion disks formed in neutron star mergers. We compute the element formation in disk outflows from hypermassive neutron star (HMNS) remnants of variable lifetime, including the effect of angular momentum transport in the disk evolution. We employ long-term axisymmetric hydrodynamic disk simulations to model the ejecta, and compute r-process nucleosynthesis with tracer particles using a nuclear reaction network containing ~ 8000 species. We find that the previously known strong correlation between HMNS lifetime, ejected mass, and average electron fraction in the outflow is directly related to the amount of neutrino irradiation on the disk, which dominates mass ejection at early times in the form of a neutrino-driven wind. Production of lanthanides and actinides saturates at short HMNS lifetimes ($\lesssim 10$ ms), with additional ejecta contributing to a blue optical kilonova component for longer-lived HMNSs. We find good agreement between the abundances from the disk outflow alone and the solar r-process distribution only for short HMNS lifetimes ($\lesssim 10$ ms). For longer lifetimes, the rare-earth and third r-process peaks are significantly under-produced compared to the solar pattern, requiring additional contributions from the dynamical ejecta. The nucleosynthesis signature from a spinning black hole (BH) can only overlap with that from a HMNS of moderate lifetime ($\lesssim 60$ ms). Finally, we show that angular momentum transport not only contributes with a late-time outflow component, but that it also enhances the neutrino-driven component by moving material to shallower regions of the gravitational potential, in addition to providing additional heating.

Key words: accretion, accretion disks — dense matter — gravitational waves — hydrodynamics — neutrinos — nuclear reactions, nucleosynthesis, abundances

1 INTRODUCTION

The astrophysical origin of chemical elements formed through the rapid neutron capture process (r-process) remains an open problem in nuclear astrophysics. Observed abundances in metal-poor Galactic halo stars demand a mechanism that produced a robust abundance pattern –

mirroring that in the Solar System – for elements with mass number $A \gtrsim 130$ (e.g., Sneden et al. 2008). This mechanism must also have operated since early on in cosmic history, since r-process elements are found in very old metal-poor stars (e.g., Cowan et al. 1999; Ji et al. 2016). In contrast, observed abundances of light r-process elements in metal-

poor stars show deviations from the solar system pattern relative to heavier elements (e.g., Montes et al. 2007). Meteoritic abundances point to different formation timescales for light and heavy r-process elements, suggesting that there might be more than one dominant formation site (Wasserburg et al. 1996).

Core-collapse supernovae may be able to produce light r-process elements ($A \lesssim 130$), but recent work indicates that they are most likely not the dominant source of heavy r-process elements (e.g., Roberts et al. 2010; Fischer et al. 2010; Hudepohl et al. 2010; Martínez-Pinedo et al. 2012; Wanajo 2013). On the other hand, mergers of binaries containing two neutron stars (NSNS) or a neutron star and a black hole (NSBH) have long been considered as candidate r-process sites, given the highly neutron-rich conditions achieved in the ejected material (Lattimer & Schramm 1974). The study of NSNS/NSBH mergers has intensified in recent years given that (1) they are likely to be detected in gravitational waves by Advanced LIGO/Virgo within the next few years (e.g., Abadie et al. 2010; LIGO Scientific Collaboration et al. 2015), (2) recent developments in numerical relativity have enabled merger simulations consistent with Einstein’s equations of general relativity (e.g., Lehner & Pretorius 2014; Paschalidis 2016), and (3) the electromagnetic signal from these events can aid with the localization of these sources and provide information complementary to that carried by gravitational waves (e.g., Rosswog 2015; Fernández & Metzger 2016; Tanaka 2016).

Recent work has shown that the dynamical ejecta from NSNS/NSBH mergers can produce a robust Solar abundance pattern for $A \gtrsim 130$ by virtue of *fission cycles* (e.g., Goriely et al. 2005), with little sensitivity to binary parameters or the equation of state (e.g., Goriely et al. 2011; Kobrin et al. 2012; Bauswein et al. 2013), depending instead on nuclear physics properties such as the fission fragment distribution (e.g., Eichler et al. 2015). When neutrino absorption is included in the calculations, a larger fraction of lighter elements ($A < 130$) can be obtained (e.g., Wanajo et al. 2014; Goriely et al. 2015; Sekiguchi et al. 2015; Radice et al. 2016; Foucart et al. 2016a,b; Roberts et al. 2017).

In addition to the dynamical ejecta, the accretion disk formed in NSNS/NSBH mergers can eject a significant amount of material on timescales longer than the dynamical time (e.g., Ruffert et al. 1997; Lee et al. 2009; Metzger et al. 2009b). The neutron-to-seed ratio of this material is lower than that in the dynamical ejecta, because the longer evolutionary timescales allow weak interactions to modify the composition more significantly (e.g., Dessart et al. 2009; Fernández & Metzger 2013; Perego et al. 2014). Matter can be ejected on the thermal timescale of the disk (~ 30 ms, §2.3) by neutrino energy deposition, or on much longer timescales (~ 1 s, §2.3) by a combination of angular momentum transport processes and nuclear recombination. The amount of mass ejected by the disk on the longer timescale can be comparable to that in the dynamical ejecta (e.g., Fernández & Metzger 2016), while the neutrino-driven component is significant only when a hypermassive neutron star (HMNS) phase precedes black hole (BH) formation (Dessart et al. 2009; Fernández & Metzger 2013; Metzger & Fernández 2014; Just et al. 2015).

Early work on nucleosynthesis from NSNS/NSBH merger disks focused on neutrino-driven outflows and used a

parametric treatment to obtain thermodynamic trajectories for composition analysis (e.g., Surman et al. 2008; Wanajo & Janka 2012), finding that conditions for both light and heavy r-process elements are possible in these outflows. More recent work has employed tracer particles from long-term hydrodynamic simulations of the disk when a BH is the central object (Just et al. 2015; Wu et al. 2016). These studies have found that the outflow generates a robust abundance of elements around $A = 130$, with significant production of lighter elements, and a variable yield of heavy r-process elements that depends on binary properties and disk physics. The case of a HMNS at the center was studied by Martin et al. (2015) using tracer particles from a time-dependent simulation that considered the neutrino-driven wind phase (Perego et al. 2014). The resulting outflow generates primarily nuclei with $A < 130$, with a significant dependence of the yield on latitude and ejection time. The long-term (viscous) outflow was not captured, however, and the lifetime of the HMNS was accounted for only by looking at subsets of particles that were ejected before a certain time.

In this study, we analyze the nucleosynthesis yields from the long-term outflow generated by an accretion disk around a HMNS of variable lifetime. Following the approach of Metzger & Fernández (2014), we conduct a number of long-term disk simulations in which the HMNS transforms into a BH at different times. This parameterized approach does not require the assumption of a particular equation of state of dense matter. It is also independent of the complex processes that determine transport of angular momentum and cooling, all of which set the survival time of the HMNS (e.g., Paschalidis et al. 2012; Kaplan et al. 2014). In order to obtain nucleosynthesis yields, tracer particles are injected in the disk initially, and the resulting thermodynamic trajectories are analyzed with the nuclear reaction network *SkyNet* (Lippuner & Roberts 2015, 2017).

This paper is structured as follows. Section 2 describes the numerical method employed and the models studied. Results are presented and discussed in section 3, and we conclude in section 4. The appendix contains further details about our numerical implementation.

2 METHODS

2.1 Disk outflow simulations and thermodynamic trajectories

The long-term evolution of the accretion disk is computed using the approach described in Metzger & Fernández (2014). In short, the equations of Newtonian hydrodynamics and lepton number conservation are solved with the FLASH code (Fryxell et al. 2000; Dubey et al. 2009) assuming axisymmetry (2D). Source terms include gravity via a pseudo-Newtonian potential, shear viscosity with an α prescription (Shakura & Sunyaev 1973), and contributions due to neutrino absorption and emission to the lepton number and energy equations. A pseudo-Newtonian potential, such as that from Artemova et al. (1996), approximates the effect of a Schwarzschild or Kerr metric by providing an innermost stable circular orbit (ISCO) in an otherwise Newtonian hydrodynamic simulation. Other aspects, such as the angular dependence of the Kerr metric, are not captured.

Neutrinos are implemented in a leakage scheme for cooling and a disk light-bulb approximation for self-irradiation. Only charged-current interactions are included, since they have the largest cross-section, exchange energy with matter, and drive the evolution of the electron fraction. The HMNS is approximated as a reflecting sphere with a radius of 30 km and a rotation period of 1.5 ms. A time-dependent, isotropic outward neutrino flux is imposed on the HMNS surface with a constant value up to 10 ms and a time dependence $t^{-1/2}$ (e.g., Pons et al. 1999) thereafter, with t being the physical simulation time. The electron neutrino and antineutrino luminosities have the same magnitude, which we normalize to $2 \times 10^{52} \text{ erg s}^{-1}$ at 30 ms, roughly matching the results of Dessart et al. (2009):

$$L_\nu = L_{\bar{\nu}} = 2\sqrt{3} \times 10^{52} \left[\max \left(1, \frac{t}{10 \text{ ms}} \right) \right]^{-1/2} \text{ erg s}^{-1}. \quad (1)$$

The neutrino and antineutrino temperatures are different, however, chosen to be 4 and 5 MeV, respectively, which roughly corresponds to the values found in proto-neutron stars in core-collapse supernovae (e.g., Janka 2001). Thus, the mean neutrino energies from the HMNS are fixed at $\langle E_\nu \rangle = 12.6 \text{ MeV}$ and $\langle E_{\bar{\nu}} \rangle = 15.8 \text{ MeV}$ (assuming a Fermi-Dirac distributions of neutrinos, the mean energy is given by $\langle E_\nu \rangle = 3.151 k_B T_\nu$, where k_B is the Boltzmann constant and T_ν is the neutrino temperature). These mean neutrino energies from the HMNS are broadly consistent with results from numerical relativity simulations that include neutrino transport (Foucart et al. 2016a). The HMNS is transformed into a BH by switching the inner radial boundary from reflecting to absorbing and setting the HMNS neutrino luminosities to zero. The viscous stress is also set to zero at this boundary when the BH forms. See Metzger & Fernández (2014) for more details.

The initial condition for most models is an equilibrium torus obtained by solving the Bernoulli equation with constant specific angular momentum and electron fraction $Y_e = 0.1$ (e.g., Papaloizou & Pringle 1984; Fernández & Metzger 2013). Outside the torus, the computational domain is filled with a low-density ambient medium that follows a power-law in radius, with an initial normalization ~ 9 orders of magnitude below the maximum torus density ($\rho_{\text{max}} \sim 10^{11} \text{ g cm}^{-3}$). The density floor inside 200 km decreases with time toward a constant asymptotic value of 10 g cm^{-3} over a timescale of $\sim 100 \text{ ms}$. In addition, one model initializes the disk using a snapshot from a general-relativistic NSBH simulation reported in Foucart et al. (2015). Details about the mapping procedure can be found in Fernández et al. (2016). Improvements to the code relative to Metzger & Fernández (2014) include the use of separate neutrino temperatures for disk self-irradiation, and a correction to the weak interaction rates; details are provided in the Appendix.

Passive tracer particles record thermodynamic quantities as a function of time, and the resulting information is used as input for the nuclear reaction network calculations (§2.2). The initial particle locations are randomly sampled to follow the mass distribution in the disk. We place 10,000 particles initially in all simulations. If there is a BH at the center, particles can fall into it, which then reduces the total number of tracer particles. Fluid quantities are obtained at each time step from the grid by linear interpolation. When

a HMNS is at the center, the reflecting boundary for particles is placed one cell outside the inner radial boundary to prevent particle trapping in a ‘trench’ of small-magnitude negative radial velocity that forms in the active cells adjacent to this boundary. The small size of this innermost radial cell relative to the inner boundary radius ($\Delta r/r \simeq 1.8\%$) ensures that the effect on the particle dynamics is minimal considering all other approximations being made.

Most hydrodynamic simulations are evolved up to about 10 s of physical time (§2.3), which is sufficient for r-process nucleosynthesis that takes place within a few seconds. To obtain the final abundances, however, the nuclear reaction network needs to be evolved for tens of years, since some of the isotopes produced by the r-process have very long half-lives. One caveat with this post-processing approach is that the energy released by the nuclear reactions does not feed back into the hydrodynamic evolution of the fluid. Nuclear heating may slightly change the morphology of the ejecta at late times (see, e.g., figure 8 of Fernández et al. 2015b) and influence specific features of the nucleosynthesis indirectly via the amount of convection in the outflow (Wu et al. 2016, see also §3.4.1).

2.2 Nuclear reaction network: *SkyNet*

We employ the nuclear reaction network *SkyNet* for the r-process nucleosynthesis calculations (Lippuner & Roberts 2015). For each thermodynamic trajectory (§2.1), we begin the reaction network evolution once the temperature falls below 10 GK or reaches its maximum, if the maximum is less than 10 GK. Since the composition is given by nuclear statistical equilibrium (NSE) at temperatures above 10 GK, there is no need to start the reaction network evolution at higher temperatures.

SkyNet includes the specific viscous heating and neutrino heating/cooling rates recorded by the thermodynamic trajectories, and adds to these a self-consistent calculation of heating from nuclear reactions. In addition to the neutrino heating/cooling rate, the associated rates of neutrino interactions with free neutrons and protons are also given by the thermodynamic trajectories and evolved in *SkyNet*. The included reactions are electron (anti) neutrino emission ($p + e^- \rightarrow n + \nu_e$, $n + e^+ \rightarrow p + \bar{\nu}_e$) and neutrino absorption ($n + \nu_e \rightarrow p + e^-$, $p + \bar{\nu}_e \rightarrow n + e^+$).

SkyNet evolves the abundances of 7843 nuclides, ranging from free neutrons and protons to ^{337}Cn , and includes over 140,000 nuclear reactions. The strong reaction rates are taken from the JINA REACLIB database (Cyburt et al. 2010), but only the forward rates are used and the inverse rates are computed from detailed balance. Spontaneous and neutron-induced fission rates are taken from Frankel & Metropolis (1947), Panov et al. (2010), Mamdouh et al. (2001), and Wahl (2002). Most of the weak rates come from Fuller et al. (1982), Oda et al. (1994), and Langanke & Martínez-Pinedo (2000) whenever they are available, and otherwise the REACLIB weak rates are used. The nuclear masses and partition functions used in *SkyNet* are taken from the WebNucleo XML file distributed with REACLIB, which contains experimental data where available and finite-range droplet macroscopic model (FRDM, see, e.g., Möller et al. 2016) data otherwise.

Table 1. List of investigated models. Columns from left to right show the model name, the compact central object (CCO) type (HMNS or BH), mass M_c of the CCO, lifetime τ of the HMNS, dimensionless spin χ of the BH (the HMNSs all spin at 1.5 ms), radius R_d of the initial disk density peak, and viscosity parameter α .

Model	CCO	M_c (M_\odot)	τ (ms)	χ	R_d (km)	α
H000	HMNS	3	0	0	50	0.03
H010			10			
H030			30			
H100			100			
H300			300			
Hinf			∞			
B070	BH	3	0	0.7	50	0.03
B090				0.9		
BF15	BH	8.1	0	0.86	55	0.03
HinfNoVisc	HMNS	3	∞	0	50	0

2.3 Investigated models

Table 1 summarizes the properties of all investigated models. The main focus of this study is the outflow from a disk around a HMNS of variable lifetime. Our baseline sequence follows the parameter choices of Metzger & Fernández (2014): a HMNS mass of $3 M_\odot$ arising from an NSNS merger, with an initial disk mass $M_d = 0.03 M_\odot$ chosen as a representative case of disk masses obtained in NSNS mergers (e.g., Hotokezaka et al. 2013). We prescribe the lifetime τ of the HMNS to be 0, 10, 30, 100, or 300 ms, after which the HMNS collapses to a non-spinning BH. We also run one case, denoted by $\tau = \infty$, in which the HMNS does not collapse. The HMNS models are denoted by H000, H010, H030, H100, H300, and Hinf, according to their lifetime. Other disk parameters are: density peak radius $R_d = 50$ km, viscosity parameter $\alpha = 0.03$, constant initial entropy of $8 k_B$ baryon $^{-1}$, constant initial $Y_e = 0.1$, and maximum evolution time of 8.7 s. These choices are motivated to be broadly compatible with results from dynamical merger simulations (e.g., Ruffert et al. 1997; Oechslin & Janka 2006; Foucart et al. 2016a) and from studies of angular momentum transport in fully-ionized accretion disks (e.g., Davis et al. 2010).

There are three important timescales in the problem: the orbital time at the initial disk density peak,

$$t_{\text{orb}} \simeq 3 \left(\frac{R_d}{50 \text{ km}} \right)^{3/2} \left(\frac{3 M_\odot}{M_c} \right)^{1/2} \text{ ms}, \quad (2)$$

where M_c is the mass of the central object (HMNS or BH); the initial thermal time in the disk,

$$t_{\text{th}} \simeq 30 \left(\frac{M_d}{0.03 M_\odot} \right) \left(\frac{e_{i,d}}{10^{19} \text{ erg g}^{-1}} \right) \left(\frac{2}{L_{\nu,52}} \right) \text{ ms}, \quad (3)$$

where $e_{i,d}$ is the initial specific internal energy of the disk (a byproduct of shock heating during the dynamical phase of the merger) and $L_{\nu,52}$ is a typical neutrino luminosity from the disk in units of $10^{52} \text{ erg s}^{-1}$ (neutrino cooling is in approximate balance with viscous heating at early times); and the initial viscous time of the disk,

$$t_{\text{visc}} \simeq 200 \left(\frac{0.03}{\alpha} \right) \left(\frac{0.3}{H/R} \right)^2 \left(\frac{R_d}{50 \text{ km}} \right)^{3/2} \left(\frac{3 M_\odot}{M_c} \right)^{1/2} \text{ ms}, \quad (4)$$

where H/R is the height-to-radius ratio of the disk. Outflows driven primarily by neutrino energy deposition are expected to be launched on the thermal timescale (equation 3), whereas long-term outflows are launched on the viscous timescale (equation 4). The latter becomes longer with time, as the disk spreads out and most of the mass in the disk resides at an increasingly larger radius (e.g., Metzger et al. 2009a). Therefore, the length of the simulations has to be several viscous timescales, which translates into thousands of orbits. We define convergence in mass ejection from the disk as a saturation in the cumulative mass crossing some radius far away from the disk (10^9 cm). This way, we generally require $3000 t_{\text{orb}}$, or about ~ 10 s for each simulation.

In order to examine the impact of the central compact object on the nucleosynthesis, we evolve two additional models with spinning BHs at the center, following the approach of Fernández et al. (2015a). The BH mass is $M_c = 3 M_\odot$ in both cases and the dimensionless spin parameter $\chi = Jc/(GM_c^2)$ is 0.7 or 0.9, where J is the BH angular momentum, c is the speed of light, and G is the gravitational constant. These models are labeled B070 and B090, according to their spin. Other parameters are the same as in the HMNS models. In addition, we investigate the effect of the disk compactness (mass of the central compact object divided by the disk density peak radius, M_c/R_d , which measures the strength of the gravitational field) by evolving a model in which the initial condition is taken from a snapshot of a general-relativistic simulation of a NSBH merger from Foucart et al. (2015), including only the remnant accretion disk. This model has a BH mass of $8.1 M_\odot$ and a disk density peak radius of 55 km, resulting in a gravitational potential that is 2.5 times stronger than our fiducial case (which better approximates the remnant of an NSNS merger). The model is denoted by BF15, and the mapping details are described in Fernández et al. (2016).

Finally, we evolve a test model that mirrors the case of a HMNS with $\tau = \infty$, but with the viscosity parameter set to zero, in order to eliminate angular momentum transport and viscous heating. This model, denoted by HinfNoVisc, experiences an outflow driven solely by neutrino heating (possibly aided by nuclear recombination), and is evolved in order to compare results with Martin et al. (2015). The model is evolved for a longer time (14.5 s) since mass ejection converges more slowly with time relative to the viscous case.

3 RESULTS AND DISCUSSION

3.1 Overview of disk evolution

The evolution of the disk and especially the neutrino interactions occurring in the disk set the stage for the outflow and determine its properties. In this section, we present a brief summary of the disk evolution, which was described in detail in Fernández & Metzger (2013) and Metzger & Fernández (2014).

When a HMNS is present, transport of angular momentum causes accreting material to form a boundary layer around the reflecting stellar surface. The outer regions of the disk expand on a thermal timescale (equation 3) due to energy injection by neutrino heating and viscous heating.

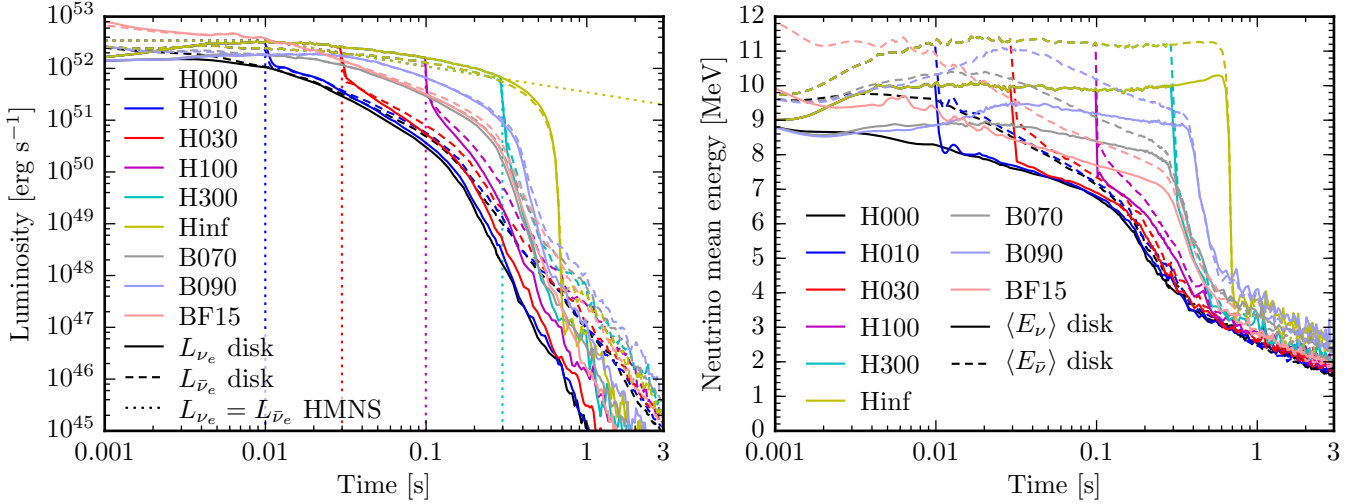


Figure 1. *Left:* Neutrino luminosities as a function of time for most models studied in this paper (see Table 1 for a summary). Shown are electron neutrinos (solid lines) and electron antineutrinos (dashed lines) emitted by the disk, as well as the imposed neutrino/antineutrino emission from the HMNS surface (dotted lines, equation 1). Sharp drops in the dotted lines mark the collapse of the HMNS into a BH. *Right:* Mean energies of electron neutrinos (solid lines) and electron antineutrinos (dashed lines) emitted by the disk. The mean energies of neutrinos and antineutrinos emitted by the HMNS are fixed at 12.6 MeV and 15.8 MeV, respectively.

Upon collapse of the HMNS to a BH, the boundary layer is swallowed, and a rarefaction wave moves outward from the inner boundary, quenching the thermal outflow (cf. Figure 3 of Metzger & Fernández 2014). The disk re-adjusts on a thermal timescale, and joins the evolutionary path of a BH accretion disk, which changes on a viscous timescale (equation 4).

The high densities achieved on the equatorial plane of HMNS disks ($\sim 10^{11} \text{ g cm}^{-3}$) are enough to locally trap neutrinos, resulting in two emission hot spots at mid latitudes and adjacent to the HMNS surface. The high densities in the midplane also result in shadowing of the outer disk, with neutrino irradiation concentrated at latitudes $\sim 30^\circ$ away from the equator (cf. Figure 2c of Metzger & Fernández 2014). This general neutrino irradiation geometry is also found when better (Monte Carlo) radiation transport is performed on snapshots of HMNS disk models (Richers et al. 2015).

The high densities near the boundary layer cause the electron fraction in the inner regions of the HMNS disk ($r < 10^7 \text{ cm}$, and within $\sim 30^\circ$ from the equatorial plane) to remain low ($Y_e \sim 0.1 - 0.2$) relative to the outer regions. Away from the midplane, the weak interaction timescale becomes shorter, and material that enters the boundary layer at high latitude reaches $Y_e \sim 0.5$ within an orbital timescale, as it transits through the hot spot in neutrino emission. Material ejected within $\sim 45^\circ$ of the rotation axis has therefore high electron fraction relative to the rest of the outflow. At $t = t_{\text{th}}$, most of the disk material within $r = 10^7 \text{ cm}$ is close to beta equilibrium, with $Y_e \sim 0.2 - 0.3$ in the outer regions. As the disk approaches a viscous timescale, the density in the inner disk gradually decreases, resulting in two effects: (1) the equilibrium Y_e of the inner disk increases as the degeneracy of the material decreases, and (2) the strength of the weak interactions decreases, until weak interactions become slow relative to the viscous time (e.g., Metzger et al. 2009a). These two effects combine to leave material close to

the HMNS with $Y_e \sim 0.4$. As long as the HMNS does not collapse, most of this material will eventually be ejected.

The BH accretion disk is such that the inner regions ($r < 10^7 \text{ cm}$) also approach beta equilibrium, but most of the material that reaches high Y_e is accreted onto the BH (cf. Figure 6 of Fernández & Metzger 2013). The fraction of the high- Y_e material that is ejected is a function of the spin of the BH, since a smaller ISCO slows down accretion and allows material to reach regions where weak interactions are stronger, before being ejected (Fernández et al. 2015a). Upon collapse of the HMNS into a BH, a low density funnel of width $\sim 45^\circ$ around the rotation axis is created as material that has not yet been unbound is swallowed. Boundary layer material reaches the highest Y_e as it crosses the emission hot spots of the HMNS disk before being ejected, hence formation of the BH precludes further ejection of material with $Y_e \sim 0.5$. For the disk masses simulated, the material becomes optically thin within a few orbits if a BH is at the center, therefore hot spots also disappear upon collapse of the HMNS.

3.2 Neutrino emission

The total electron neutrino and antineutrino luminosities from the disk and the HMNS (if present) as a function of time are shown in the left panel of Figure 1. The disk luminosities are very similar to the luminosity from the HMNS as long as the latter does not collapse, because the disk absorbs and re-radiates the neutrinos emitted by the HMNS. When the HMNS collapses, the disk luminosities undergo a sudden decrease, and then follow a broken powerlaw as the disk re-adjusts and continues to evolve on the viscous timescale. Thereafter, $L_{\bar{\nu}_e}$ starts to dominate over L_{ν_e} in all models because the initial neutron-rich ($Y_e = 0.1$) composition of the disk causes weak interactions to leptonize it, with more positron captures than electron captures (the gradual drop in density over the viscous timescale increases the equilib-

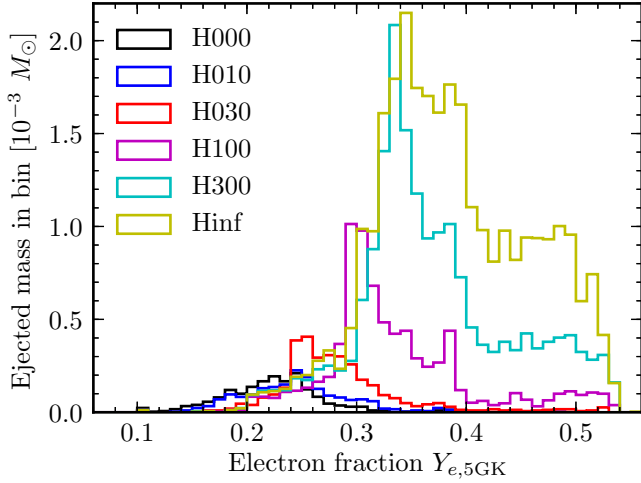


Figure 2. Mass distribution of the ejecta electron fraction for HMNS models at the time when the temperature is ≥ 5 GK for the last time for each tracer particle.

rium Y_e of the disk; §3.1). As long as the HMNS is present, the disk neutrino luminosities are approximately the same in all cases, consistent with re-radiation of the HMNS luminosities, and the different models are separated by a shift in time depending on the lifetime of the HMNS.

The mean neutrino energies emitted by the disk are shown in the right panel of Figure 1. Given the low initial abundance of protons, the optical depth for antineutrinos is initially low, and antineutrino energies are higher by $\sim 10\%$ than neutrino energies until $t \sim t_{\text{visc}}$, by which time the decrease in disk density has gradually lifted the degeneracy and weak interactions have driven the inner disk close to $Y_e \sim 0.4$. The neutrino/antineutrino energies are the same between HMNS models until the HMNS collapses, each following the same general evolution pattern but shifted in time. Since the disk mostly re-radiates neutrinos from the HMNS, the mean neutrino energies drop sharply when the HMNS collapses.

In the models that start out with a BH at the center (B070, B090, BF15, and H000, which has $\chi = 0$), a more rapidly spinning BH results in higher neutrino luminosities and mean neutrino energies. This occurs because larger spins are associated with smaller ISCO radii. Hence the disk material can convert more gravitational energy into thermal energy, resulting in more intense neutrino emission with higher mean energies. In model BF15, the central BH is more massive ($8.1 M_\odot$ compared to $3 M_\odot$ in H000, B070, and B090), which results in a larger ISCO radius. The disk has nearly the same density peak radius as the other models, but the initial condition is not in equilibrium. Therefore, accretion proceeds more intensely at early times than in the other BH models, speeding up the disk evolution despite its slightly longer initial viscous time (smaller H/R in equation 4, which overcomes the effect of a larger BH mass).

3.3 Ejecta properties

In order to associate the thermodynamic properties of the disk with the nucleosynthesis outcome from each trajectory, we use the value of the electron fraction ($Y_{e,5\text{GK}}$) and spe-

cific entropy ($s_{5\text{GK}}$) at the last time when the temperature of the tracer particle drops below 5 GK. For the rare cases in which the temperature of the trajectory is always below 5 GK, we use the initial values of Y_e and s for $Y_{e,5\text{GK}}$ and $s_{5\text{GK}}$, respectively. Once the temperature drops below approximately 5 GK, the composition moves out of NSE and a full network evolution is required to evolve the abundances. Therefore $Y_{e,5\text{GK}}$ and $s_{5\text{GK}}$ are the initial conditions for nucleosynthesis. Note that the reaction network evolution starts when the temperature drops below 10 GK, but *SkyNet* can also evolve the composition while NSE holds.

The distribution of mass ejected as a function of $Y_{e,5\text{GK}}$ is shown in Figure 2 for all HMNS models with non-zero viscosity. A trajectory is considered to have been ejected when it crosses the surface $r = 10^9$ cm. There is a strong correlation between the HMNS lifetime and both the amount of mass ejected and the mean $Y_{e,5\text{GK}}$ of the distribution (Metzger & Fernández 2014). The disk ejecta ranges from 6 to nearly 100% of the initial disk mass. The longer the HMNS lives, the longer the disk material is subject to strong neutrino heating, which combines with viscous heating and nuclear recombination to eject material on the viscous timescale. A longer HMNS lifetime also allows more material from the inner disk to be ejected instead of being swallowed by the BH. That material from the inner disk reaches beta equilibrium and hence its ejection results in a higher mean electron fraction. Table 2 shows the number of ejected particles (out of the initial 10,000 particles in each model) and the total ejected mass. Also shown is the amount of mass ejected with $Y_{e,5\text{GK}} \leq 0.25$, which is neutron-rich enough to robustly make the full r-process (see next section and, e.g., Lippuner & Roberts 2015).

We note that the amount of mass ejected with $Y_{e,5\text{GK}} \leq 0.25$ is roughly constant between $(0.5 - 0.8) \times 10^{-3} M_\odot$ once the HMNS lives for 30 ms or longer, despite the total ejecta mass differing by an order of magnitude. This is the result of two competing effects: a longer HMNS lifetime increases the total ejecta mass, but it also increases the average electron fraction of the ejecta, thus reducing the fraction of the ejected mass that has $Y_{e,5\text{GK}} \leq 0.25$. These two effects counteract each other, leaving the absolute amount of mass ejected with $Y_{e,5\text{GK}} \leq 0.25$ roughly constant.

The thermodynamic properties of the ejecta for model H300 (HMNS with lifetime $\tau = 300$ ms) are illustrated in Figure 3 through the electron fraction $Y_{e,5\text{GK}}$, specific entropy $s_{5\text{GK}}$, final velocity v_{final} , ejecta mass, and the time $t_{5\text{GK}}$ when the temperature is 5 GK for the last time. Two ejecta components stand out from the scatter plot of $Y_{e,5\text{GK}}$ versus $s_{5\text{GK}}$. The larger component is ejected before the HMNS collapses, i.e. $t_{5\text{GK}} \lesssim 300$ ms, and it exhibits a tight correlation between the entropy and electron fraction up to $Y_{e,5\text{GK}} \sim 0.5$. This is indicative of a neutrino-driven wind, and indeed we would expect the asymptotic Y_e to be ~ 0.55 based on the neutrino properties shown in Figure 1 (Qian & Woosley 1996). Note that the vast majority of the ejecta with $Y_{e,5\text{GK}} \gtrsim 0.4$ or $v_{\text{final}} \gtrsim 0.03 c$ is part of this early wind-like ejecta, with a much smaller group of particles extending to low velocities and low electron fractions.

The second component is ejected after the HMNS has collapsed to a BH, i.e. $t_{5\text{GK}} \gtrsim 300$ ms, and it has only a weak correlation between $Y_{e,5\text{GK}}$ and $s_{5\text{GK}}$. This component is associated with mass ejection as the disk reaches the advective

Table 2. Summary of nucleosynthesis results. N_{ej} is the number of tracer particles that reach a radius $r = 10^9$ cm by the end of the hydrodynamic simulation (every simulation starts with 10,000 particles); M_{ej} is the total ejected mass in $10^{-3} M_{\odot}$ at the same radius; $M(Y_e \leq 0.25)$ is the ejected mass with $Y_{e,5\text{GK}} \leq 0.25$; $M_{\nu\text{-driv}}$ is the amount of ejected mass that is driven by neutrino interactions; $[Y_{1\text{st}}/Y_{2\text{nd}}]$ is the \log_{10} of the ratio of the first r-process peak to the second r-process peak, normalized to the solar value, see Equation (5) for details; $[Y_{\text{RE}}/Y_{2\text{nd}}]$ and $[Y_{3\text{rd}}/Y_{2\text{nd}}]$ are the same quantities for the rare-earth and third peaks; $\langle X_{\text{La}} \rangle$ and $\langle X_{\text{Ac}} \rangle$ are the lanthanide and actinide mass fractions averaged over all ejecta particles; and $\epsilon_{\text{tot}} 1 \text{ d}$ and $\epsilon_{\text{tot}} 7 \text{ d}$ are the total heating rates of the entire ejecta at 1 and 7 days, respectively.

Model	N_{ej}	M_{ej} ($M_{-3\odot}$)	$M(Y_e \leq 0.25)$ ($M_{-3\odot}$)	$M_{\nu\text{-driv}}$ ($M_{-3\odot}$)	$[Y_{1\text{st}}/Y_{2\text{nd}}]$	$[Y_{\text{RE}}/Y_{2\text{nd}}]$	$[Y_{3\text{rd}}/Y_{2\text{nd}}]$	$\langle X_{\text{La}} \rangle$	$\langle X_{\text{Ac}} \rangle$	$\epsilon_{\text{tot}} 1 \text{ d}$ (erg s^{-1})	$\epsilon_{\text{tot}} 7 \text{ d}$ (erg s^{-1})
H000	527	1.8	1.4	0.013	-1.3	-0.28	-0.30	4.6×10^{-2}	6.4×10^{-3}	9.0×10^{40}	1.4×10^{40}
H010	557	1.9	1.1	0.027	-1.1	-0.40	-0.50	3.3×10^{-2}	2.0×10^{-3}	8.9×10^{40}	1.3×10^{40}
H030	989	3.3	0.83	0.20	-0.64	-1.0	-1.2	5.1×10^{-3}	2.9×10^{-4}	1.2×10^{41}	1.5×10^{40}
H100	2408	7.8	0.52	1.3	-0.0053	-0.91	-1.2	2.1×10^{-3}	1.7×10^{-4}	1.8×10^{41}	1.4×10^{40}
H300	5610	18	0.67	6.4	+0.25	-0.88	-1.2	1.1×10^{-3}	6.7×10^{-5}	3.3×10^{41}	3.2×10^{40}
Hinf	9587	30	0.69	28*	+0.41	-0.86	-1.1	7.1×10^{-4}	4.2×10^{-5}	5.2×10^{41}	5.4×10^{40}
B070	1465	5.4	1.8	0.022	-0.73	-0.65	-0.67	1.3×10^{-2}	1.6×10^{-3}	2.0×10^{41}	2.4×10^{40}
B090	2363	7.9	1.6	0.070	-0.54	-0.77	-0.80	7.6×10^{-3}	9.7×10^{-4}	2.7×10^{41}	2.6×10^{40}
BF15	910	4.9	0.011	0.022	-0.26	-1.4	-1.3	1.4×10^{-3}	7.7×10^{-5}	7.8×10^{40}	6.7×10^{39}

* Since the HMNS persists forever in model Hinf, virtually all trajectories experience significant neutrino interactions and our method becomes inadequate to isolate the component of the ejecta that is driven by neutrino interactions.

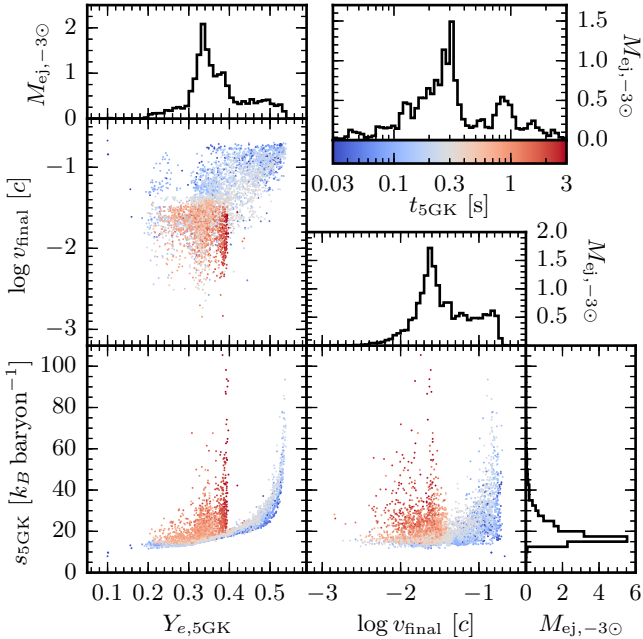


Figure 3. Properties of the ejecta of model H300 (central HMNS that collapse after 300 ms). $Y_{e,5\text{GK}}$ and $s_{5\text{GK}}$ are the electron fraction and specific entropy at the time $t_{5\text{GK}}$, when the temperature of the trajectory is 5 GK for the last time, while v_{final} is the final velocity of the trajectory. The scatter plot points are color coded by $t_{5\text{GK}}$, which marks the nucleosynthesis starting time. Blue and gray points ($t_{5\text{GK}} \lesssim 300$ ms) start their nucleosynthesis while the HMNS is present, and are thus influenced by the neutrino irradiation from the HMNS. The strong correlation between electron fraction and entropy is similar to what is obtained in a neutrino-driven outflow. The red points ($t_{5\text{GK}} \gtrsim 300$ ms) start nucleosynthesis after the HMNS has collapsed to a BH. Hence this component is subject primarily to the action of viscous processes and nuclear recombination in the disk. See the text for details. $M_{\text{ej},-3\odot}$ means the amount of ejecta mass in units of $10^{-3} M_{\odot}$.

tive state (very weak or no neutrino cooling/heating) and is driven primarily by heat injection from angular momentum transport processes and nuclear recombination (Metzger & Fernández 2014). Mass ejection in this state is accompanied by vigorous convective activity in the disk.

In order to quantitatively disentangle the wind-like ejecta component seen in Figure 3 from the other component, we compute the contributions to $s_{5\text{GK}}$ arising from neutrino and viscous heating. While all trajectories experience some degree of viscous heating, only a subset of tracer particles experience an entropy change due to neutrino heating that is larger than $0.1 k_B \text{ baryon}^{-1}$ (ignoring any neutrino cooling). And that subset exactly exhibits the tight, boomerang-shaped correlation between $Y_{e,5\text{GK}}$ and $s_{5\text{GK}}$ that the early, wind-like ejecta exhibits (cf. the blue and gray dots in the lower left panel of Figure 3). The mass of this neutrino-driven ejecta component is shown in Table 2 under $M_{\nu\text{-driv}}$. This component is absent for HMNS lifetimes shorter than 30 ms and also in the BH models, but once the HMNS lifetime becomes longer, the neutrino-driven component becomes as large or even the dominant fraction of the total ejecta (such as in model Hinf, in which almost the entire ejecta is neutrino-driven). For very long-lived HMNSs all trajectories experience some degree of neutrino interactions, and it becomes difficult to distinguish the wind-like from the viscous component. We emphasize that even the neutrino-driven component experiences significant viscous heating and the entropy change due to viscous heating can be of the same order as that due to neutrino absorption.

One interesting feature of the late-time component is the sharp upper limit of $Y_{e,5\text{GK}} \sim 0.38 - 0.40$, regardless of entropy. These trajectories experience late-time fall back due to large convective eddies in the disk. They get sucked deep inside the disk where the density is much higher than in the outflow, and then they are ejected again almost immediately. This creates a spike in their density profile that results in significant heating, as evidenced by the fact that they all have $T \geq 5$ GK at $t \sim 2$ s. However, before this late-time heating occurs, r-process nucleosynthesis has already taken place in these trajectories, and all free neutrons have been captured

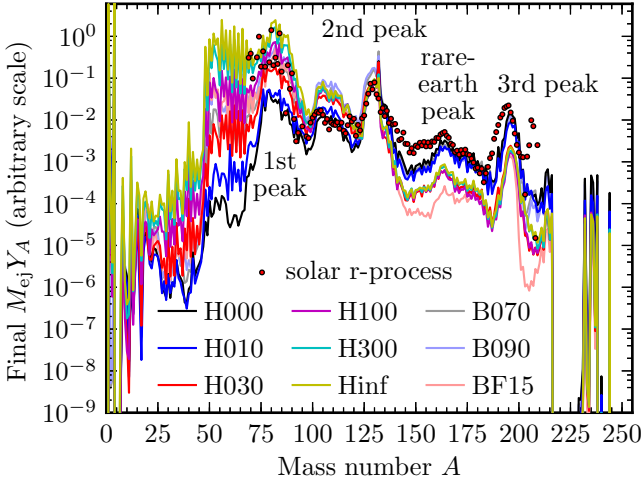


Figure 4. Final trajectory-averaged abundances as a function of mass number, scaled by the total ejecta mass, for all models with non-zero viscosity. The observed solar r-process abundances (Arnould et al. 2007) are scaled to match the second peak of the HMNS models at $A = 130$ (none of the abundances from our models have been scaled).

onto seed nuclei. Thus, the composition before the heating spike consists of heavy elements with β -decay half-lives of milliseconds to seconds. These elements decay and raise the overall electron fraction of the material to $Y_e \sim 0.38 - 0.40$, which is the characteristic Y_e at 1–3 seconds after neutron exhaustion for the r-process, for a wide range of initial Y_e . The late-time heating then simply pushes the material back into NSE, but the electron fraction remains unchanged. The resulting entropy depends on the amount of heating received by each trajectory, as determined by how far the material falls back into the disk. This class of trajectories therefore ends up with electron fractions $Y_{e,5\text{GK}} \sim 0.38 - 0.40$ and nucleosynthesis start times of $t_{5\text{GK}} \sim 2$ s, with uncorrelated entropies.

3.4 Nucleosynthesis

3.4.1 Final abundances

The mass-averaged composition of the ejecta for all models with non-zero viscosity is shown in Figure 4. The abundances are multiplied by the total ejecta mass to emphasize their relative contributions to the different r-process regions. Models H000 and H010 (prompt non-spinning BH and shortest-lived HMNS, respectively) agree most closely with the Solar System r-process abundances (Arnould et al. 2007), which have been scaled to match the second peak at $A = 130$ (the abundances from our models have not been scaled). The abundances around the third r-process peak in these two models approach the solar values, whereas in all other models production of the third peak is too low compared to solar. H000 and H010 also have the best agreement with the solar rare-earth peak around $A \sim 165$. While these two models under-produce the first r-process peak ($A \sim 80$), they agree rather well with the feature around $A \sim 100$, in contrast to all other models which over-produce it.

While the good agreement between models H000/H010 and the solar r-process abundances could be taken as an in-

dication of short HMNS lifetimes being more common, one has to keep in mind that Figure 4 assumes that the entire second solar r-process peak is due to the disk outflow. Other sources such as the dynamical ejecta from NSNS/NSBH mergers and core-collapse supernovae can also produce significant amounts of r-process elements. The expected abundance patterns are weighted toward the third peak for the dynamical ejecta (e.g., Goriely et al. 2011; Wanajo et al. 2014; Roberts et al. 2017) and toward the first peak for core-collapse supernovae (e.g., Wanajo 2013; Shibagaki et al. 2016; Vlasov et al. 2017). The solar r-process abundance is thus the outcome of the contribution from each source weighted by their rate and yield per event.

In all models, the third peak is shifted to slightly higher mass numbers, which is a well-known shortcoming of the FRDM mass model (e.g., Mendoza-Temis et al. 2015; Mumpower et al. 2016). We also see an abundance spike at $A = 132$ in all models. This spike is due to some trajectories experiencing late-time heating that photodissociates neutrons from synthesized heavy elements. This results in additional neutron capture and a pile up of material at the doubly magic nucleus ^{132}Sn ($N = 82$ and $Z = 50$). Wu et al. (2016) also observed this phenomenon and described it in detail.

The models with longer HMNS lifetimes have less neutron-rich ejecta (Figure 2) and hence synthesize a greater fraction of first peak material. Once the HMNS lifetime is longer than 100 ms, the first peak ($70 \leq A \leq 90$) is over-produced with respect to the solar values, when the abundances are normalized to the second peak. Again, we emphasize that the r-process yield from disk outflows is complementary to that from the dynamical ejecta, which tends to produce more neutron-rich nuclei.

We quantify the relative contribution of each model to the different regions of the r-process distribution by computing average abundances around the peaks and normalizing them to the solar values. The abundance of the second peak $Y_{2\text{nd}}$ is computed as the sum of the abundances in the range $125 \leq A \leq 135$, excluding $A = 132$ to avoid the spike at that mass number. For the first peak abundance $Y_{1\text{st}}$, we use the sum of abundances in the range $70 \leq A \leq 90$. For the rare-earth peak Y_{RE} , we use $160 \leq A \leq 166$ and for the third peak we use $186 \leq A \leq 203$. The quantity $[Y_{1\text{st}}/Y_{2\text{nd}}]$ shown in Table 2 is defined as

$$[Y_{1\text{st}}/Y_{2\text{nd}}] = \log_{10} \frac{Y_{1\text{st}}}{Y_{2\text{nd}}} - \log_{10} \frac{Y_{1\text{st},\odot}}{Y_{2\text{nd},\odot}}, \quad (5)$$

where $Y_{1\text{st},\odot}$ and $Y_{2\text{nd},\odot}$ are the abundances of the third and second peak as observed in the solar system, respectively. The same procedure is used to compute $[Y_{\text{RE}}/Y_{2\text{nd}}]$ and $[Y_{3\text{rd}}/Y_{2\text{nd}}]$. Using the solar r-process abundances from Arnould et al. (2007), we find $\log Y_{1\text{st},\odot}/Y_{2\text{nd},\odot} = +1.3$, $\log Y_{\text{RE},\odot}/Y_{2\text{nd},\odot} = -1.1$, and $\log Y_{3\text{rd},\odot}/Y_{2\text{nd},\odot} = -0.42$, which we use to normalize the values shown in Table 2.

The different peak ratios shown in Table 2 quantify the trends apparent in Figure 4. For models H000 and H010, the rare-earth and third peaks are under-produced by only a third to one half of an order of magnitude. But the first peak is under-produced by slightly more than an order of magnitude compared to the second peak in those models. As we go to longer HMNS lifetimes, the rare-earth and third peaks are under-produced by about an order of magnitude

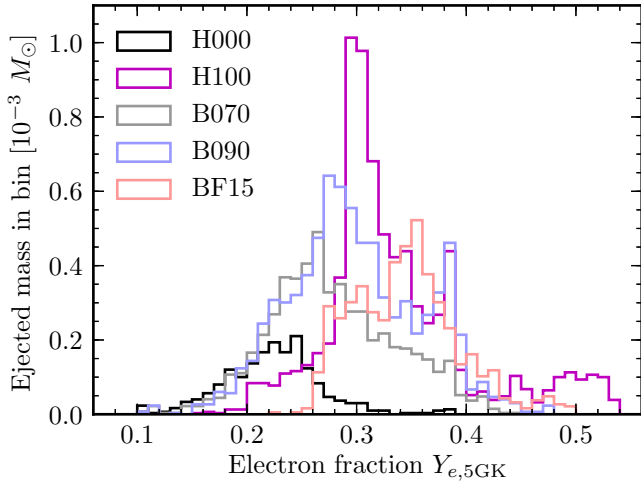


Figure 5. Mass histograms of electron fraction for the ejecta from BH models. We include the HMNS model H100 for comparison.

regardless of the HMNS lifetime. At the same time, the first peak increases from an under-production of 2/3 of an order of magnitude at $\tau = 30$ ms to an over-production of a factor of 2.6 at $\tau = \infty$.

The spinning BH models under-produce the first, rare-earth, and third peaks in roughly the same amounts, namely between about half to 3/4 of an order of magnitude compared to the second peak. The compact disk model BF15 under-produces the third peak by a similar amount as the HMNS models with long lifetimes. But it also has the lowest rare-earth peak abundance relative to solar, with an under-production factor of about 1.5 orders of magnitude. The first peak, on the other hand, is only under-produced by a factor of ~ 2 .

3.4.2 BH spin mimicking HMNS lifetime

Metzger & Fernández (2014) proposed using the relative amount of blue optical emission in the kilonova as an observational test of the HMNS lifetime, given that the latter correlates with the amount of high- Y_e material ejected in the disk outflow. Given that high- Y_e material also correlates with BH spin (Fernández et al. 2015a), the kilonova signature of the two types of central objects can overlap. Here we investigate whether the nucleosynthesis signature offers additional information that can break the degeneracy. We consider the BH models H000, B070, and B090, which have the same mass and varying spins $\chi = 0, 0.7$, and 0.9 , respectively, as well as model BF15, which has a larger mass and $\chi = 0.86$. Figure 5 shows the electron fraction distributions of these BH models.

While a larger BH spin has a similar overall effect on the disk ejecta composition as a longer HMNS lifetime, even a spin $\chi = 0.9$ does not reach the same amount of ejecta mass and average value of $Y_{e,5GK}$ as a HMNS with a lifetime $\tau = 100$ ms (cf. Figure 5). At best, a rapidly spinning BH can mimic a HMNS of modest lifetime. This can also be seen in Figure 4 and in the peak ratio values in Table 2. Models B070 and B090 have values of $[Y_{1st}/Y_{2nd}]$ that are similar or slightly smaller than in model H030, while the values of $[Y_{RE}/Y_{2nd}]$ and $[Y_{3rd}/Y_{2nd}]$ from models B070 and

B090 fall between those from models H010 and H030. Thus, a BH with a spin $\chi = 0.7 - 0.9$ produces a disk outflow with a similar final abundance pattern as a HMNS with a lifetime of $\tau \sim 15 - 20$ ms. Therefore, the fact that we assume a non-spinning BH after collapse of the HMNS only has a very small impact on the nucleosynthesis. Model BF15, on the other hand, looks more like a HMNS with a lifetime $\tau \sim 60$ ms, judging from the under-production of the first and third peaks relative to the second peak. Nonetheless, the rare-earth peak is under-produced by almost half an order of magnitude more in the disk ejecta by BF15 than by the HMNS models with long lifetimes.

3.4.3 Lanthanides, actinides, and heating rates

The energy released by the radioactive decay of heavy elements synthesized by the r-process can power an optical or infrared transient called a kilonova (also called macronova in the literature; Li & Paczyński 1998; Kulkarni 2005; Metzger et al. 2010; Roberts et al. 2011; Kasen et al. 2013). The two most important microphysical components that determine the light curve and spectrum of kilonovae are the opacity of the material and the radioactive heating rate. Lanthanides ($58 \leq Z \leq 71$) and actinides ($90 \leq Z \leq 103$) have open f-shells, which gives them a very complex atomic line structure that leads to broadband opacities that are more than an order of magnitude larger than opacities from iron-group elements (Kasen et al. 2013; Tanaka & Hotokezaka 2013; Fontes et al. 2015).

The trajectory-averaged lanthanide ($\langle X_{La} \rangle$) and actinide ($\langle X_{Ac} \rangle$) mass fractions of the ejecta for all models are summarized in Table 2. For HMNS lifetimes $\tau \leq 10$ ms, the lanthanide mass fraction is a few times 10^{-2} , which will result in opacities about an order of magnitude larger than iron group opacities (see Figure 10 in Kasen et al. 2013). Note that the actinide mass fractions are on the order of 10^{-3} , which is still a significant contribution to the opacity. Once the HMNS lifetime is longer than about 10 ms, the lanthanide fraction $\langle X_{La} \rangle \sim 10^{-3}$ monotonically decreases as the lifetime increases. In these models, the lanthanides and actinides will increase the opacity only by a factor of a few relative to iron group opacities. In the BH models, increasing the spin from 0.7 to 0.9 reduces the lanthanide and actinide mass fractions by roughly a factor of two from around 10^{-2} . The compact disk model BF15 has very similar lanthanide and actinide mass fractions as H300. These results apply to the disk outflow component alone; the color of a kilonova depends also on the spatial distribution and composition of the dynamical ejecta, which tends to be more neutron-rich and hence may contain significant amounts of lanthanides and actinides.

Figure 6 shows the combined lanthanide and actinide mass fraction of each ejected trajectory as a function of $Y_{e,5GK}$ for models H010, Hinf, B090, and BF15. For most trajectories, the lanthanide and actinide fraction plummets as the initial electron fraction increases from 0.2 to 0.25 (see also Lippuner & Roberts 2015; Kasen et al. 2015). Particles with $Y_{e,5GK} \leq 0.25$ have low entropies, because a higher entropy requires either significant neutrino heating, which increases Y_e , or viscous heating over timescales comparable to the thermal time, which gives weak interactions enough time to increase Y_e toward its equilibrium value. This corre-

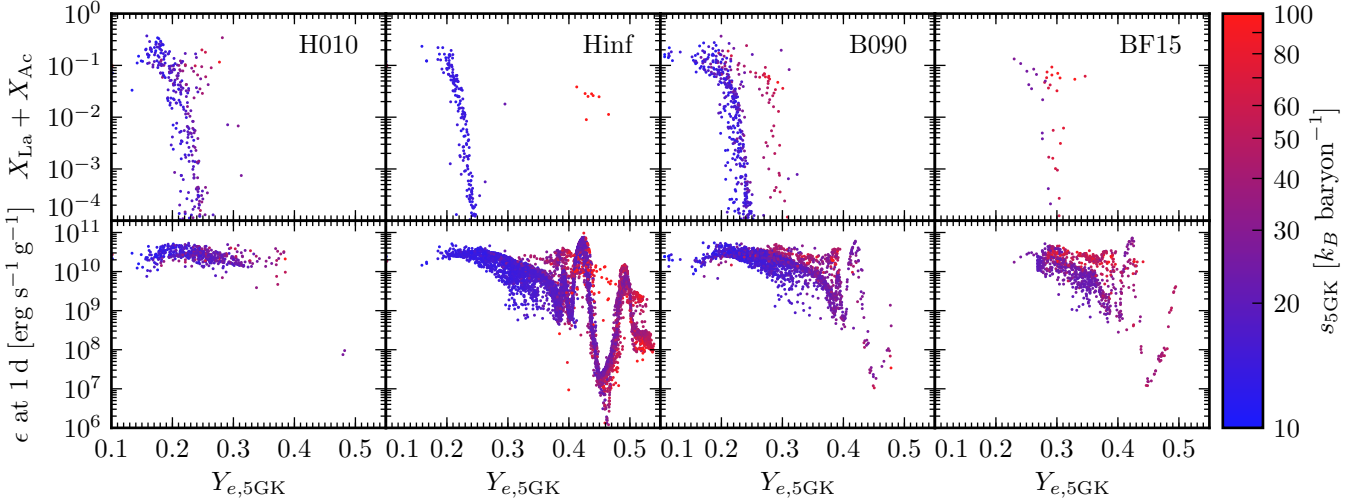


Figure 6. *Top:* Scatter plots of final lanthanide and actinide mass fraction in each trajectory as a function of the electron fraction $Y_{e,5GK}$, for selected models. Points are color-coded by the initial entropy s_{5GK} . *Bottom:* Radioactive heating rate ϵ at one day as a function of $Y_{e,5GK}$, also color-coded by s_{5GK} .

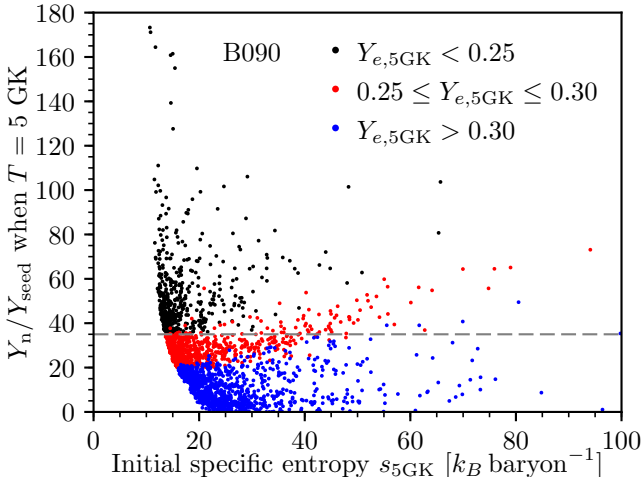


Figure 7. Neutron-to-seed ratio at the time when the temperature $T \geq 5$ GK for the last time, versus the specific entropy at that time, for ejected trajectories from model B090. Nuclides with $A \geq 12$ are counted as seeds. The gray dashed line indicates the minimum value of $Y_n/Y_{seed} = 35$ that is required to make lanthanides and actinides. All trajectories with $Y_{e,5GK} < 0.25$ (black dots) are above the minimum neutron-to-seed ratio regardless of initial entropy, while almost all trajectories with $Y_{e,5GK} > 0.30$ (blue dots) are below it. The remaining trajectories ($0.25 \leq Y_{e,5GK} \leq 0.30$, red dots) can produce lanthanides or actinides if the initial entropy is $\gtrsim 30 - 40 k_B \text{ baryon}^{-1}$.

lation between $Y_{e,5GK}$ and s_{5GK} at $Y_{e,5GK} \lesssim 0.3$ can be seen in Figure 3.

Figure 6 also shows that there is a separate population of particles that contain significant amounts of lanthanides and actinides for electron fractions in the range $0.25 \lesssim Y_{e,5GK} \lesssim 0.3$, particularly in models B090, BF15, and to a lesser extent in model H010. This group of trajectories has higher entropies ($s_{5GK} \gtrsim 30 k_B \text{ baryon}^{-1}$) relative to those which do not make lanthanides or actinides for $Y_{e,5GK} \geq 0.25$. We can understand this pop-

ulation by considering the strong dependence of the lanthanide/actinide abundance on the neutron-to-seed ratio Y_n/Y_{seed} , where $Y_{seed} = \sum_{A \geq 12} Y_A$. In general, a neutron-to-seed ratio $Y_n/Y_{seed} \sim 40$ is necessary to produce a significant amount of lanthanides and actinides: as Y_n/Y_{seed} increases from about 35 to about 45, $X_{La} + X_{Ac}$ increases from $\sim 10^{-5}$ to $\sim 10^{-2}$. This effect is illustrated in Figure 7 for model B090, where the different particle populations are shown in different colors. The trajectories in the range $Y_{e,5GK} = 0.25 - 0.30$ lie on both sides of the $Y_n/Y_{seed} = 35$ boundary for the range of entropies encountered in the disk ejecta, with a critical entropy for lanthanide production $s_{5GK} \sim 30 - 40 k_B \text{ baryon}^{-1}$. Outside of this range of Y_e , lanthanide production is insensitive to s_{5GK} . The neutron-to-seed ratio increases with increasing entropy because a higher entropy prefers a larger number of particles, and thus the composition contains more lighter particles such as free neutrons.

The population of trajectories with $Y_{e,5GK} = 0.25 - 0.30$ and $s_{5GK} \gtrsim 30 k_B \text{ baryon}^{-1}$ is absent in model Hinf (cf. Figure 6). In order to achieve such entropies at modest electron fraction, neutrino irradiation cannot be too strong. In model Hinf, the weak interaction timescale is comparable to the viscous heating timescale, raising Y_e above 0.3. Since the HMNS is the strongest source of neutrinos while it persists, this population of trajectories can only exist if there is either no HMNS or if the HMNS collapses to a BH quickly. The eight trajectories in model Hinf that produce lanthanides and actinides at $Y_{e,5GK} \gtrsim 0.4$ are an extreme case. They all have $s_{5GK} > 200 k_B \text{ baryon}^{-1}$, which allows the neutron-to-seed ratio to be high enough to make lanthanides and actinides even at $Y_e > 0.4$. These particles attain this high entropy because of late-time fallback into (and then rapid ejection from) the innermost part of the disk, where they experience significant heating past 5 GK.

Table 2 gives the total radioactive heating rate in the ejecta ϵ_{tot} at 1 day and at 7 days for all models. The quantity scales with the total ejecta mass. When considering the contribution of the disk outflow to a radioactively-powered

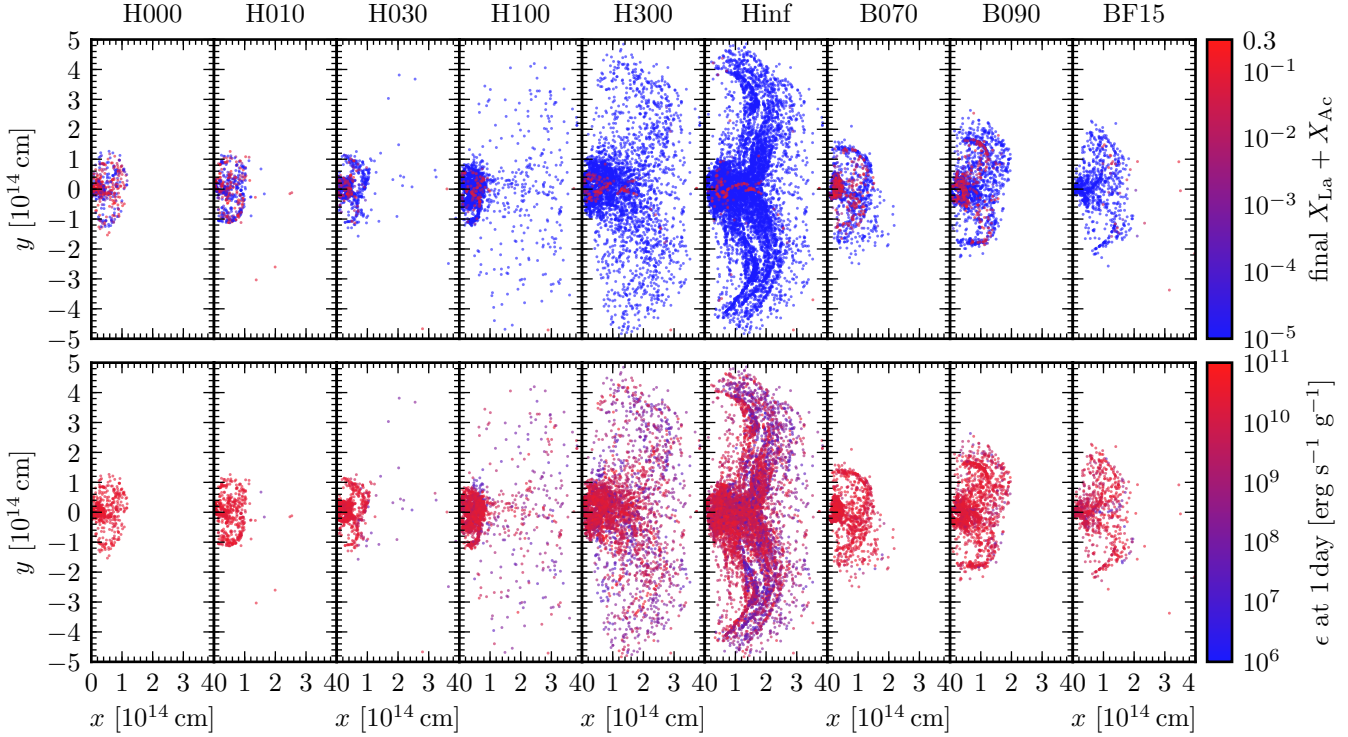


Figure 8. Spatial distribution of ejected trajectories at time $t = 1$ day, for all HMNS and BH models with non-zero viscosity. Positions are computed by assuming that the velocity of each particle at the end of the simulation (~ 10 s) remains constant at later times. Aside from smoothing of sharp features by radioactive heating at late times (Rosswog et al. 2014; Fernández et al. 2015b), this extrapolation of trajectories yields a good first approximation to the morphology of the homologously expanding disk wind ejecta. *Top:* Final lanthanide and actinide mass fraction. Because the high-lanthanide component of the ejecta is very small in most models, the points with $X_{\text{La}} + X_{\text{Ac}} \geq 10^{-3}$ are plotted above all other points with lower mass fractions (except for models H000 and H010). The lanthanide and actinide mass fractions stop changing a few seconds after neutrons are exhausted. Therefore, the final mass fractions are the same as the ones prevailing during the kilonova emission phase. *Bottom:* Radioactive heating rate at one day. In this row, the points for the different trajectories are drawn in a random order for all models.

kilonova, we need to keep in mind the contribution of the dynamical ejecta, which is not simply additive as in the case of nucleosynthesis. The larger fraction of lanthanides and actinides expected for the dynamical ejecta means that its optical opacity is likely to be larger than that of the disk outflow. The geometry of the dynamical ejecta depends on the type of merger involved: quasi-spherical for NSNS mergers (e.g., Hotokezaka et al. 2013), or confined to the equatorial plane for NSBH mergers (e.g., Kawaguchi et al. 2015; Foucart et al. 2017). In the former case, the disk ejecta can be obstructed in all directions by high-opacity material, whereas in the latter a long-lasting blue optical component from the disk ejecta can be detectable from some directions (Kasen et al. 2015). A short-lived blue optical component should be detectable in most cases since the lanthanide-rich material goes through a high-temperature phase and its outer layers let photons escape more freely (Barnes & Kasen 2013; Fernández et al. 2016).

If we only consider the heating rates and lanthanide/actinide content from the disk outflow, we expect models H000 and H010 to make dim infrared kilonovae, while all other models should make bright blue optical kilonovae. The exception is B070, which has about 1.5% lanthanides and actinides by mass and a fairly large heating rate, so this model could make a brighter infrared kilonova. The heating rates reported here are upper limits to the bol-

ometric luminosities of kilonovae from the disk outflow, since the conversion of energy from radioactive decay products into thermal energy of the ejecta has a limited efficiency (e.g., Metzger et al. 2010; Hotokezaka et al. 2016; Barnes et al. 2016).

The bottom row of Figure 6 shows the heating rates of the individual trajectories at $t = 1$ day as a function of $Y_{e,5\text{GK}}$. The heating rate decreases slowly with increasing electron fraction for $Y_{e,5\text{GK}} \lesssim 0.3$. For higher initial Y_e , the decrease steepens until large oscillations start around $Y_{e,5\text{GK}} \sim 0.4$. This general behavior is consistent with the findings of the parametrized r-process nucleosynthesis study of Lippuner & Roberts (2015). The oscillations are due to the initial NSE composition, which can be dominated by a small number of individual nuclei that match the electron fraction of the material. If there is a nuclide with a matching Y_e that has a half-life of about a day, there will be strong heating at $t \sim 1$ day as this nuclide decays, but if there is no such nuclide, then there will be significantly less heating. The peak in the heating rate at $Y_{e,5\text{GK}} \sim 0.425$, visible in all but the first column of Figure 6, is caused by ^{66}Ni , which has $Y_e = 28/66 \sim 0.424$ and is a dominant nuclide in the initial NSE composition. ^{66}Ni decays to ^{66}Cu with a half-life of 55 hours, which then decays to stable ^{66}Zn with a half-life of 5 minutes. Around $Y_{e,5\text{GK}} \sim 0.45$, there is a large dip in the heating rate because the initial composition

is dominated by ^{62}Ni and ^{66}Zn , both of which are stable and have $Y_e = 0.45$. The little neutron capture that takes place mainly builds up ^{88}Sr , which is also stable and has $Y_e = 0.43$. At $Y_{e,5\text{GK}} \sim 0.49$ there is another peak in the heating rate due to ^{62}Zn , ^{61}Cu , and ^{57}Ni , which are all unstable and very abundant since they have electron fractions between 0.48 and 0.49. At higher entropies, the initial neutron to seed ratio is enhanced, which will generally produce unstable nuclei and thus possibly break the oscillatory pattern of heating rate versus $Y_{e,5\text{GK}}$.

The morphology of the ejecta for all models with non-zero viscosity is shown in Figure 8, with the top row showing final lanthanide and actinide mass fractions. Since the material is close to homologous expansion, Figure 8 essentially shows the velocity space distribution of the ejected particles. In all models, most of the particles are concentrated in a central blob. When the HMNS persists for 100 ms or more, some particles attain higher velocities ($v \sim 0.1c$) and organize themselves into multiple shells (which arise from *shock trains* in the gas; e.g., Matsuo et al. 1999). Since particles are accelerated to high velocities predominantly by neutrino irradiation, there are more high-velocity particles the longer the HMNS persists.

In some models (H000, H010, and B070) there appears to be little structure in the distribution of lanthanides and actinides. In others there is a clear preference for the high-lanthanide trajectories to be at low velocities and clustered in the equatorial plane. Model BF15 is an exception in that the few particles that make a significant amount of lanthanides and actinides achieve the highest velocities, because they experienced a significant amount of heating (cf. Figure 6). The few high-entropy trajectories in model Hinf that make lanthanides and actinides at $Y_{e,5\text{GK}} \gtrsim 0.4$ are the high-velocity points moving predominantly in the polar direction, i.e., they have a large absolute y coordinate and a small x coordinate in Figure 8. For the heating rates, on the other hand, there is no strong spatial correlation between heating magnitude and trajectory location in any of the models. Models H300 and Hinf are the only ones which have a significant component of low heating rate trajectories, although these particles follow the same velocity distribution as those with high heating rates. Note that the low-heating particles are easier to see in the outer part of the ejecta because the lower particle density, but they are also present in the central blob.

3.4.4 Comparison with *r*-process abundances in metal-poor halo stars

Metal-poor galactic halo stars that show *r*-process elements in their spectra are thought to have been enriched by a single or few *r*-process nucleosynthesis events (Cowan et al. 1999). Figure 9 shows the final elemental abundances (at $t \sim 10$ Myr) of our investigated models, along with the solar *r*-process abundances from Arnould et al. (2007) and from four metal-poor halo stars as reported in Westin et al. (2000) and Roederer et al. (2012). Abundances are scaled to give the best possible match to the solar values in the range $56 \leq Z \leq 75$. There is little variation between the different models in this range, and a generally good match to solar and metal-poor star abundances. While Eu ($Z = 63$) is under-produced by a factor of a few with respect to solar

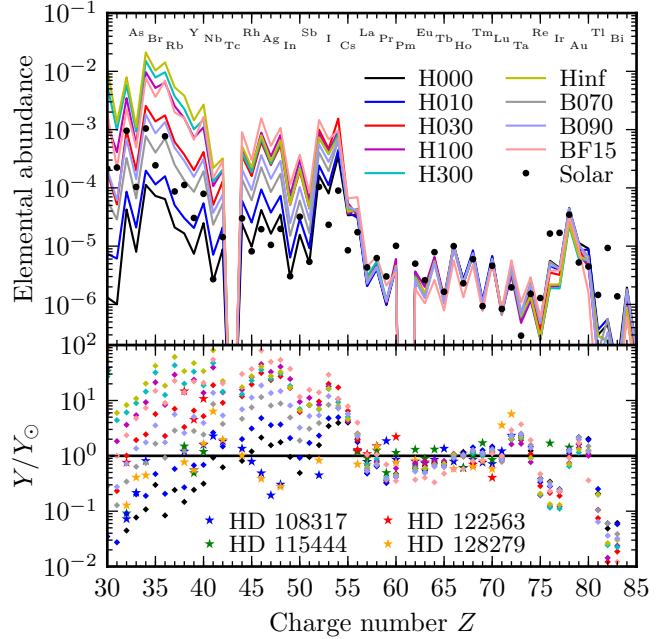


Figure 9. *Top:* Final elemental abundances for all models with non-zero viscosity. In each case, abundances are scaled so that $\sum (\log Y_Z/Y_{Z,\odot})^2$ is minimized for $55 \leq Z \leq 75$. Black dots show solar system *r*-process abundances (Arnould et al. 2007). *Bottom:* Ratio of model abundances to solar system *r*-process abundances (diamonds). Also shown are the observed abundances of four metal-poor halo stars (shown as stars, from Westin et al. 2000; Roederer et al. 2012), scaled to the solar system values in the same way as model abundances.

in our models, the metal-poor halo stars also exhibit slightly sub-solar Eu abundances.

Regarding elements in the range $44 \leq Z \leq 55$, Figure 9 shows that they are overproduced relative to the solar values by all models except H000. In the range $Z = 30 - 42$, our disk outflow models do not match the solar abundances, but nonetheless agree with the overall increase in abundances with Z (compared to solar) exhibited by metal-poor halo stars. From $Z = 44$ to 47, the metal-poor halo stars have a declining abundance trend compared to solar, which none of our models reproduce. In fact, the disk outflow generates an increasing trend from $Z = 44$ to 47. Thus, we can conclude that both the solar and metal-poor halo stars' abundance patterns are inconsistent with pure disk outflow nucleosynthesis. This means that the nucleosynthesis event (or events) that enriched these metal-poor halo stars in heavy *r*-process elements could not have been the *r*-process in merger disk outflow alone. There must have been contributions from additional types of ejecta, or perhaps a different kind of nucleosynthesis event altogether. Contributions from very neutron-rich dynamical ejecta that produces mainly second to third peak material ($Z \gtrsim 55$) could make the combined final abundance pattern consistent with the metal-poor halo star observations (cf. Just et al. 2015). For $Z \lesssim 42$, we expect supernovae to contribute to the nucleosynthesis, thus making it difficult to draw any conclusions from the disk outflow nucleosynthesis alone.

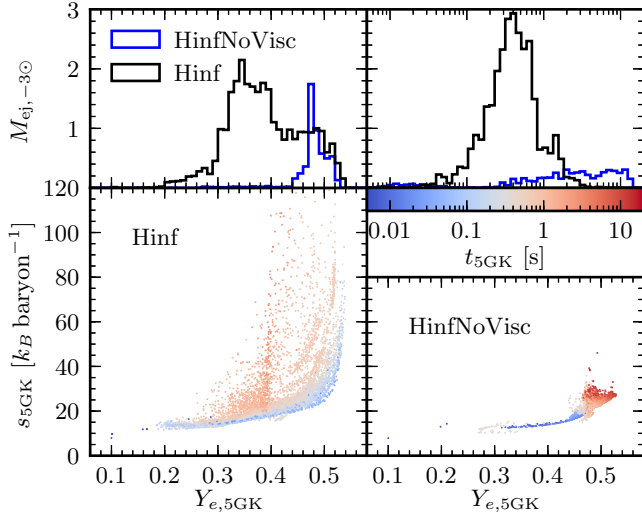


Figure 10. Properties of the disk wind ejecta from a HMNS that does not collapse, including and excluding the effect of viscosity on angular momentum transport and heating (models Hinf and HinfNoVisc, respectively). *Top:* Histograms of the ejected mass in units of $10^{-3} M_{\odot}$ as a function of $Y_{e,5GK}$ (left) and as a function of the time t_{5GK} when each particle has cooled to 5 GK (right). *Bottom:* Scatter plot of $Y_{e,5GK}$ versus s_{5GK} , color-coded by t_{5GK} for model Hinf (left) and HinfNoVisc (right).

3.5 Impact of angular momentum transport

Neutrino irradiation from a HMNS is strong enough that significant amounts of material can in principle be ejected by neutrino energy deposition alone (Ruffert et al. 1997). Therefore, it is useful to clarify the contribution of angular momentum transport processes to the overall mass ejection from the disk. Transport of angular momentum modifies the evolution of the disk in two ways: (1) it causes part of the disk to accrete and part to spread outward as the local contribution of centrifugal forces to hydrostatic balance is modified, and (2) it dissipates energy in the form of heat, increasing the local entropy of the gas. While the detailed form of these two effects depends on the way the process is modeled (i.e. α viscosity), the overall contribution to the disk evolution is generic (e.g., magnetohydrodynamic turbulence also heats up the gas, but with a different spatial distribution than shear viscosity; e.g., Hirose et al. 2006).

We focus here on two models of a HMNS which does not collapse: one including angular momentum transport through α viscosity like all other models (Hinf), and another in which the viscosity is set to zero (HinfNoVisc). Figure 10 shows the distribution of the ejected particles as a function of initial electron fraction $Y_{e,5GK}$, initial specific entropy s_{5GK} , and nucleosynthesis start time (t_{5GK}).

A non-zero viscosity increases the total ejecta mass from $5.5 \times 10^{-3} M_{\odot}$ (HinfNoVisc) to $29.6 \times 10^{-3} M_{\odot}$ (Hinf), which corresponds to 18% and 99% of the initial disk mass, respectively. Not all of this additional mass is directly ejected by angular momentum transport, however. The scatter plot of $Y_{e,5GK}$ versus s_{5GK} in Figure 10 shows a clear neutrino-driven wind pattern for part of the ejecta from model Hinf (see also §3.3 and Figure 3). This pattern is associated primarily with the early ejecta ($t_{5GK} \lesssim 0.2$ s), which covers the range $Y_{e,5GK} = 0.2 - 0.54$. Some particles that start nucle-

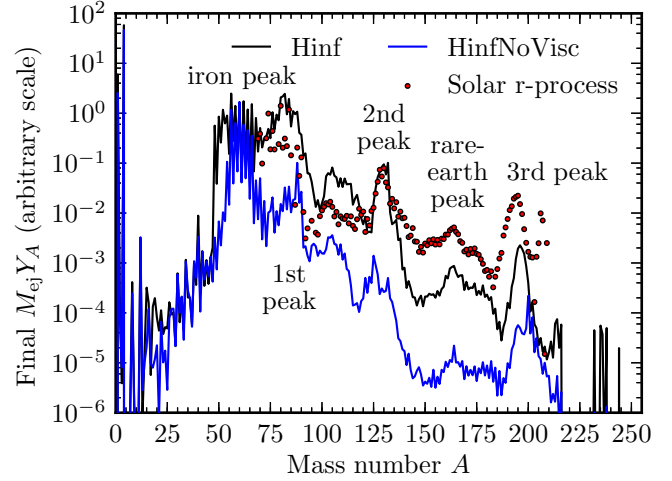


Figure 11. Final abundances of non-collapsing HMNS models with and without viscosity (Hinf and HinfNoVisc, respectively). Model abundances are scaled by the total ejecta mass of each model, while the solar system r-process abundances (Arnould et al. 2007) are scaled to match the second peak of model Hinf.

osynthesis later ($t_{5GK} \sim 0.5$ s), with electron fractions in the range $Y_{e,5GK} = 0.4 - 0.54$, also exhibit strong correlations between $Y_{e,5GK}$ and s_{5GK} . This later ejecta could thus also be neutrino-driven, but the different thermodynamic conditions prevailing at later times alter the exact relationship between $Y_{e,5GK}$ and s_{5GK} . Ejecta that begins nucleosynthesis at later times ($t_{5GK} \gtrsim 0.8$ s), with $Y_{e,5GK} = 0.3 - 0.4$, shows a much larger dispersion in s_{5GK} for a given $Y_{e,5GK}$. This dispersion is associated with convective motions in the advective phase of the disk, in which mass ejection is driven exclusively by viscous heating and nuclear recombination (§3.3).

In contrast, Figure 10 shows that the model with zero viscosity ejects almost exclusively material with $Y_{e,5GK} = 0.47 - 0.52$, with ejection happening predominantly at late times ($t_{5GK} \gtrsim 1$ s). All of the trajectories in model HinfNoVisc exhibit the characteristic neutrino-driven wind correlation between electron fraction and entropy. Given that the model with viscosity has more neutrino-driven wind ejecta than model HinfNoVisc, we infer that angular momentum transport not only adds an additional late-time ejecta component, but it also enhances the neutrino-driven wind itself. This enhancement arises from two effects. First, spreading of the outer regions of the disk due to angular momentum transport moves material into shallower regions of the gravitational potential, where thermal unbinding requires less energy injection. Second, viscous heating also acts on the neutrino-driven wind ejecta, increasing the rate of internal energy gain. This also explains why the neutrino-driven component is delayed in the case without viscosity: particles are more tightly bound, requiring energy deposition for a longer time in order to be ejected.

Figure 11 shows the final abundances for models Hinf and HinfNoVisc. Without viscosity, most of the ejecta has $Y_{e,5GK} \sim 0.5$, and so the final abundance is dominated by the iron peak ($A \sim 56$) and ${}^4\text{He}$. Note that HinfNoVisc produces the same iron peak and ${}^4\text{He}$ abundance as Hinf despite its total ejecta mass being more than a factor of

five lower. For elements significantly heavier than the iron peak, the final abundance of model HinfNoVisc is one to two orders of magnitude lower than in model Hinf. While model HinfNoVisc can still make the third r-process peak, the material is produced by just a handful of particles that have $Y_{e,5\text{GK}} \leq 0.25$.

The nucleosynthesis in the disk outflow from a HMNS has also been studied by Martin et al. (2015), who focused on the neutrino-driven wind without the contribution from angular momentum transport. In their study, they use the ejection time of a particle as a proxy for the HMNS lifetime. Martin et al. find that the total ejecta mass increases with increasing HMNS ejection time, and that the ejecta also becomes less neutron-rich at later times. These results are broadly consistent with what we find in model HinfNoVisc.

A more detailed comparison between the results from Martin et al. and ours shows that the initial disk mass can have a significant impact on the properties of this ejecta component. Martin et al. find most of the ejecta having $Y_e \sim 0.3 - 0.4$, and a majority of the particles ejected on a timescale of 100 ms, whereas model HinfNoVisc has $Y_e \sim 0.5$ and most trajectories begin nucleosynthesis after 1 s. The initial condition in Martin et al. is the output of a three-dimensional neutron star merger simulation by Perego et al. (2014), with a disk that is more than six times as massive as in our model ($0.19 M_\odot$ compared to $0.03 M_\odot$). Different physical and thermodynamic conditions in the disk can lead to different results in the nucleosynthesis (e.g., compare the output of our models B070 with BF15). Another source for the differences in the ejecta properties can be the different hydrodynamic methods used, which can have different amounts of numerical viscosity. Finally, one similarity between the results of Martin et al. and ours is the characteristic values for the entropy in the neutrino-driven wind ($\sim 20 k_B$ baryon $^{-1}$; compare the bottom right panel of Figure 10 and Figure 5 in Martin et al. 2015).

4 CONCLUSIONS

We have performed nucleosynthesis calculations in the outflow from a neutron star merger accretion disk when the central object is a HMNS or a BH. We used long-term hydrodynamic simulations of accretion disks to model the ejecta, and detailed nucleosynthesis calculations were carried out on tracer particles using a nuclear reaction network. We have systematically varied the lifetime of the central HMNS to study its impact on the nucleosynthesis. Our simulations continued after the HMNS collapses to a BH, thus allowing us to investigate the long-term effects on the disk and nucleosynthesis. We have also performed some simulations that start with central BHs with different spins, to explore similarities and differences with the HMNS case.

Our results are consistent with previous findings regarding the monotonic increase in mass ejection and mean electron fraction of the disk outflow for longer HMNS lifetimes (Figure 2; see also Metzger & Fernández 2014). This correlation results in the amount of ejecta that has initial $Y_e \leq 0.25$ being almost constant once the HMNS lifetime is $\tau \gtrsim 30$ ms. The final abundance pattern at large mass numbers ($A \gtrsim 100$), normalized by the total ejecta mass, is thus independent of the HMNS lifetime, because only ma-

terial with $Y_e \lesssim 0.25$ can make those heavy elements (Figure 4). For very short HMNS lifetimes ($\tau \lesssim 10$ ms), there is more neutron-rich ejecta and thus the rare-earth and third r-process abundance peaks are about half an order of magnitude larger. For these short lifetimes, the disk outflow abundances alone are almost consistent with the solar r-process abundances.

For other cases, the inconsistency between the final abundances from the disk outflow and the solar values is not in itself problematic. In most neutron star mergers, we also expect a dynamical ejecta component that tends to be more neutron-rich. This means it could easily synthesize the heavy r-process material that the disk ejecta may be under-producing. If the dynamical ejecta is consistent with the solar r-process abundances between the second and third peak, then our results indicate a preference for short HMNS lifetimes, since abundances from these models are broadly consistent with solar r-process abundances between the second and third peak. If, on the other hand, the dynamical ejecta over-produces the third peak relative to the second peak, then we would require longer HMNS lifetimes, which result in under-production of the third peak compared to the second, in order to make the combined abundance pattern consistent with solar. We draw similar conclusions from comparing the nucleosynthesis in our disk models to the observed abundances in metal-poor halo stars (Figure 9).

If the HMNS lifetime is $\tau \gtrsim 30$ ms, most of the ejected material has $Y_e \gtrsim 0.25$ and so only a small amount of lanthanides and actinides are synthesized. Thus we expect that the disk outflow to produce a kilonova that peaks in the optical band on a timescale of a day. However, this optical kilonova component may be obscured by lanthanides and actinides that were synthesized in the more neutron-rich dynamical ejecta; the effect might be viewing-angle dependent (cf. Kasen et al. 2015). If the HMNS lifetime is 10 ms or less, then the disk outflow contains substantial amounts of lanthanides and actinides. This would also produce an infrared kilonova on a timescale of a week and would probably be indistinguishable from the dynamical ejecta contribution. The properties of the radioactive heating rates from our tracer particles (Figure 6) are consistent with the findings of Lippuner & Roberts (2015). We find no strong spatial correlation between radioactive heating and particle location in the ejecta (Figure 8).

By comparing the disk outflow abundances when a spinning BH or a HMNS is the central object, we find that a BH of spin 0.7–0.9 can mimic a HMNS with lifetime $\tau \sim 15$ ms. If the central BH is more massive (and the disk is compact, such as in a NSBH remnant), then it can mimic a longer-lived HMNS with $\tau \sim 60$ ms. For longer HMNS lifetimes ($\tau \gtrsim 100$ ms), we find no possible overlap between the amounts of mass ejected or the nucleosynthesis signatures. Determining whether this difference translates into the kilonova signature requires more detailed radiation transport calculations using realistic initial conditions for the central object, disk, and dynamical ejecta.

Regarding the disk outflow dynamics, we find that when a HMNS is present, two types of ejecta are clearly distinguishable: one driven primarily by neutrino energy deposition, showing a clear correlation between electron fraction and entropy, and another driven primarily by viscous heating and nuclear recombination, in which no such cor-

relation exists (Figure 3). We evolved a test model with no explicit angular momentum transport, and found that the contribution of viscosity is not limited to the late-time neutrino-independent outflow. Angular momentum transport also aids the ejection of the neutrino-driven component by moving material to shallower regions of the gravitational potential, and by accelerating thermal ejection through additional heating of the gas (Figure 10). Thus, excluding angular momentum transport in the HMNS disk evolution can severely underestimate the amount of mass ejected.

Neutrino interactions in the disk play a crucial role in setting the electron fraction and specific entropy distributions of the outflow. Likewise, the dominance of the HMNS irradiation in driving the early outflow requires a realistic treatment of the merger remnant instead of its approximation as a reflecting boundary. Hence our approximate treatment of the HMNS surface and neutrino interactions are the most important limitations of this study. While we are confident that the results and trends found in this study are robust, we nevertheless plan to use more sophisticated neutrino radiation transport methods in future work. Incorporating an α viscosity prescription into our disk simulations is a significant step forward from simulations with no physical viscosity. Ultimately, however, accretion disk simulations with more realistic physical viscosity (e.g., provided by magnetoturbulence driven by the magnetorotational instability) need to be performed. Furthermore, due to the extreme computational complexity of fully general-relativistic hydrodynamics simulations, no self-consistent simulations of neutron star mergers with subsequent long-term accretion disk evolution have been carried out to date. Our approach of assuming an initial equilibrium torus is thus a necessary approximation in order to investigate nucleosynthesis in merger accretion disks. Mapping the early accretion disk structure found in merger simulations into another code for the disk evolution (as we have done for model BF15) is a more accurate approach, but it is still not fully self-consistent. With next generation general-relativistic hydrodynamics codes, we hope to be able to perform completely self-consistent simulations of neutron star mergers and accretion disk outflows in the future. Finally, we only use the FRDM nuclear mass model for the nucleosynthesis calculations in this study. In future work, we plan to investigate and compare other nuclear mass models for r-process nucleosynthesis in disk outflows.

ACKNOWLEDGMENTS

JL and CDO acknowledge support from NSF grant AST-1333520. RF acknowledges support from the University of California Office of the President, from NSF grant AST-1206097, and from the Faculty of Science at the University of Alberta. DK is supported in part by a Department of Energy Office of Nuclear Physics Early Career Award, and by the Director, Office of Energy Research, Office of High Energy and Nuclear Physics, Divisions of Nuclear Physics, of the U.S. Department of Energy under Contract No. DE-AC02-05CH11231. The software used in this work was in part developed by the DOE NNSA-ASC OASCR Flash Center at the University of Chicago. This research used resources of the National Energy Research Scientific Computing Center

(NERSC), which is supported by the Office of Science of the U.S. Department of Energy under Contract No. DE-AC02-05CH11231. Some computations were performed on the *Edison* compute cluster (repository m2058). Some of the calculations were performed on the *Zwicky* compute cluster at Caltech, supported by NSF under MRI award PHY-0960291 and by the Sherman Fairchild Foundation. This work was supported in part by NSF grant PHY-1430152 (JINA Center for the Evolution of the Elements). CDO thanks the Yukawa Institute for Theoretical Physics for support and hospitality. This article has been assigned Yukawa Institute report number YITP-17-26.

APPENDIX A: IMPROVEMENTS TO THE HYDRODYNAMIC DISK SIMULATIONS

We have corrected an error in the weak interaction rates used since Fernández & Metzger (2013). The error involved the absence of the neutron-proton mass difference in the argument of the Fermi-Dirac integrals for all the electron neutrino rates (but not in the antineutrino rates). After correction of this error, the electron neutrino emission rates decrease by a factor of up to two in regions with temperatures $\gtrsim 1$ MeV. The most significant change in the result is an increase in the fraction of matter ejected with $Y_e > 0.25$ for the non-spinning BH case from a few percent to $\sim 30\%$ of the outflow, resulting in an increase of $\sim 10\%$ in the average Y_e of the outflow. A similar increase in the mean Y_e of the wind is observed for the long-lived HMNS case. In terms of the amount of mass ejected, the effects are strongest for a non-spinning BH, which ejects up to $\sim 10\%$ more mass than before the correction is applied (i.e. an additional $\sim 0.5\%$ of the initial disk mass). For a long-lived HMNS, the mass ejection increases by $\sim 0.2\%$.

Relative to Metzger & Fernández (2014), we also account for separate neutrino and antineutrino temperatures for absorption. The mean energy for each neutrino species is calculated by taking the ratio of the globally-integrated energy to number emission rates, as in Ruffert et al. (1996). The temperatures are then obtained through the relation $kT_{\nu,i} = F_4(0)/F_5(0)\langle\varepsilon_{\nu,i}\rangle$, where F_i are the Fermi-Dirac functions of integer argument, $F_5(0)/F_4(0) \simeq 5.065$, and $\langle\varepsilon_{\nu,i}\rangle$ is the neutrino mean energy. When using the updated weak interaction tables, this change translates into an *increase* of $\sim 10\%$ in mass ejection for a non-spinning BH, and a *decrease* of 0.4% in mass ejection for a long-lived HMNS.

To put the effect of these modifications in perspective for the non-spinning BH case, doubling the resolution of the simulations in each dimension can change mass ejection by $\sim 10\%$ (Fernández et al. 2015b), and a change in the α viscosity parameter leads to an almost directly proportional change in mass ejection (i.e., a factor ten when going from $\alpha = 0.01$ to $\alpha = 0.1$, Wu et al. 2016).

REFERENCES

- Abadie, J., Abbott, B. P., Abbott, R., et al., 2010, CQG, 27, 173001, doi:10.1088/0264-9381/27/17/173001
- Arnould, M., Goriely, S., & Takahashi, K., 2007, Phys. Rep., 450, 97, doi:10.1016/j.physrep.2007.06.002

- Artemova, I. V., Bjoernsson, G., & Novikov, I. D., 1996, *ApJ*, 461, 565, doi:10.1086/177084
- Barnes, J. & Kasen, D., 2013, *ApJ*, 775, 18, doi:10.1088/0004-637X/775/1/18
- Barnes, J., Kasen, D., Wu, M.-R., & Martínez-Pinedo, G., 2016, *ApJ*, 829, 110, doi:10.3847/0004-637X/829/2/110
- Bauswein, A., Goriely, S., & Janka, H.-T., 2013, *ApJ*, 773, 78, doi:10.1088/0004-637X/773/1/78
- Cowan, J. J., Pfeiffer, B., Kratz, K.-L., et al., 1999, *ApJ*, 521, 194, doi:10.1086/307512
- Cybert, R. H., Amthor, A. M., Ferguson, R., et al., 2010, *ApJS*, 189, 240, REACLIB is available at <https://groups.nsl.msu.edu/jina/reaclib/db/>, doi:10.1088/0067-0049/189/1/240
- Davis, S. W., Stone, J. M., & Pessah, M. E., 2010, *ApJ*, 713, 52, doi:10.1088/0004-637X/713/1/52
- Dessart, L., Ott, C. D., Burrows, A., Rosswog, S., & Livne, E., 2009, *ApJ*, 690, 1681, doi:10.1088/0004-637X/690/2/1681
- Dubey, A., Reid, L. B., Weide, K., et al., 2009, *Parallel Comput.*, 35, 512, doi:10.1016/j.parco.2009.08.001
- Eichler, M., Arcones, A., Kelic, A., et al., 2015, *ApJ*, 808, 30, doi:10.1088/0004-637X/808/1/30
- Fernández, R., Foucart, F., Kasen, D., et al., 2016, submitted to *CQG*, arXiv:astro-ph.HE/1612.04829
- Fernández, R., Kasen, D., Metzger, B. D., & Quataert, E., 2015a, *MNRAS*, 446, 750, doi:10.1093/mnras/stu2112
- Fernández, R. & Metzger, B. D., 2013, *MNRAS*, 435, 502, doi:10.1093/mnras/stt1312
- Fernández, R. & Metzger, B. D., 2016, *Annual Review of Nuclear and Particle Science*, 66, annurev-nucl-102115-044819, doi:10.1146/annurev-nucl-102115-044819
- Fernández, R., Quataert, E., Schwab, J., Kasen, D., & Rosswog, S., 2015b, *MNRAS*, 449, 390, doi:10.1093/mnras/stv238
- Fischer, T., Whitehouse, S. C., Mezzacappa, A., Thielemann, F.-K., & Liebendörfer, M., 2010, *A&A*, 517, A80, doi:10.1051/0004-6361/200913106
- Fontes, C. J., Fryer, C. L., Hungerford, A. L., et al., 2015, *High Energy Density Physics*, 16, 53, doi:10.1016/j.hedp.2015.06.002
- Foucart, F., Desai, D., Brege, W., et al., 2017, *Classical and Quantum Gravity*, 34, 044002, doi:10.1088/1361-6382/aa573b
- Foucart, F., Haas, R., Duez, M. D., et al., 2016a, *PRD*, 93, 044019, doi:10.1103/PhysRevD.93.044019
- Foucart, F., O'Connor, E., Roberts, L., et al., 2015, *PRD*, 91, 124021, doi:10.1103/PhysRevD.91.124021
- Foucart, F., O'Connor, E., Roberts, L., et al., 2016b, *PRD*, 94, 123016, doi:10.1103/PhysRevD.94.123016
- Frankel, S. & Metropolis, N., 1947, *Physical Review*, 72, 914, doi:10.1103/PhysRev.72.914
- Fryxell, B., Olson, K., Ricker, P., et al., 2000, *ApJS*, 131, 273, doi:10.1086/317361
- Fuller, G. M., Fowler, W. A., & Newman, M. J., 1982, *ApJS*, 48, 279, doi:10.1086/190779
- Goriely, S., Bauswein, A., & Janka, H.-T., 2011, *ApJL*, 738, L32, doi:10.1088/2041-8205/738/2/L32
- Goriely, S., Bauswein, A., Just, O., Pllumbi, E., & Janka, H.-T., 2015, *MNRAS*, 452, 3894, doi:10.1093/mnras/stv1526
- Goriely, S., Demetriou, P., Janka, H.-T., Pearson, J. M., & Samyn, M., 2005, *Nuclear Physics A*, 758, 587, doi:10.1016/j.nuclphysa.2005.05.107
- Hirose, S., Krolik, J. H., & Stone, J. M., 2006, *ApJ*, 640, 901, doi:10.1086/499153
- Hotokezaka, K., Kiuchi, K., Kyutoku, K., et al., 2013, *PRD*, 87, 024001, doi:10.1103/PhysRevD.87.024001
- Hotokezaka, K., Wanajo, S., Tanaka, M., et al., 2016, *MNRAS*, 459, 35, doi:10.1093/mnras/stw404
- Hüdepohl, L., Müller, B., Janka, H.-T., Marek, A., & Rafelt, G. G., 2010, *Physical Review Letters*, 104, 251101, doi:10.1103/PhysRevLett.104.251101
- Janka, H.-T., 2001, *A&A*, 368, 527, doi:10.1051/0004-6361:20010012
- Ji, A. P., Frebel, A., Chiti, A., & Simon, J. D., 2016, *Nature*, 531, 610, doi:10.1038/nature17425
- Just, O., Bauswein, A., Pulpillo, R. A., Goriely, S., & Janka, H.-T., 2015, *MNRAS*, 448, 541, doi:10.1093/mnras/stv009
- Kaplan, J. D., Ott, C. D., O'Connor, E. P., et al., 2014, *ApJ*, 790, 19, doi:10.1088/0004-637X/790/1/19
- Kasen, D., Badnell, N. R., & Barnes, J., 2013, *ApJ*, 774, 25, doi:10.1088/0004-637X/774/1/25
- Kasen, D., Fernández, R., & Metzger, B. D., 2015, *MNRAS*, 450, 1777, doi:10.1093/mnras/stv721
- Kawaguchi, K., Kyutoku, K., Nakano, H., et al., 2015, *PRD*, 92, 024014, doi:10.1103/PhysRevD.92.024014
- Korobkin, O., Rosswog, S., Arcones, A., & Winteler, C., 2012, *MNRAS*, 426, 1940, doi:10.1111/j.1365-2966.2012.21859.x
- Kulkarni, S. R., 2005, preprint, astro-ph/0510256, arXiv:astro-ph/0510256
- Langanke, K. & Martínez-Pinedo, G., 2000, *Nucl. Phys. A*, 673, 481, doi:10.1016/S0375-9474(00)00131-7
- Lattimer, J. M. & Schramm, D. N., 1974, *ApJ*, 192, L145, doi:10.1086/181612
- Lee, W. H., Ramirez-Ruiz, E., & López-Cámara, D., 2009, *ApJL*, 699, L93, doi:10.1088/0004-637X/699/2/L93
- Lehner, L. & Pretorius, F., 2014, *ARA&A*, 52, 661, doi:10.1146/annurev-astro-081913-040031
- Li, L.-X. & Paczyński, B., 1998, *ApJL*, 507, L59, doi:10.1086/311680
- LIGO Scientific Collaboration, Aasi, J., Abbott, B. P., et al., 2015, *CQG*, 32, 074001, doi:10.1088/0264-9381/32/7/074001
- Lippuner, J. & Roberts, L. F., 2015, *ApJ*, 815, 82, doi:10.1088/0004-637X/815/2/82
- Lippuner, J. & Roberts, L. F., 2017, in preparation
- Mamdouh, A., Pearson, J. M., Rayet, M., & Tondeur, F., 2001, *Nuc. Phys. A*, 679, 337, doi:10.1016/S0375-9474(00)00358-4
- Martin, D., Perego, A., Arcones, A., et al., 2015, *ApJ*, 813, 2, doi:10.1088/0004-637X/813/1/2
- Martínez-Pinedo, G., Fischer, T., Lohs, A., & Huther, L., 2012, *Physical Review Letters*, 109, 251104, doi:10.1103/PhysRevLett.109.251104
- Matsuo, K., Miyazato, Y., & Kim, H.-D., 1999, *Progress in Aerospace Sciences*, 35, 33, doi:10.1016/S0376-0421(98)00011-6
- Mendoza-Temis, J. d. J., Wu, M.-R., Langanke, K., et al., 2015, *PRC*, 92, 055805, doi:10.1103/PhysRevC.92.055805
- Metzger, B. D. & Fernández, R., 2014, *MNRAS*, 441, 3444, doi:10.1093/mnras/stu802

- Metzger, B. D., Martínez-Pinedo, G., Darbha, S., et al., 2010, *MNRAS*, 406, 2650, doi:10.1111/j.1365-2966.2010.16864.x
- Metzger, B. D., Piro, A. L., & Quataert, E., 2009a, *MNRAS*, 396, 304, doi:10.1111/j.1365-2966.2008.14380.x
- Metzger, B. D., Piro, A. L., & Quataert, E., 2009b, *MNRAS*, 396, 1659, doi:10.1111/j.1365-2966.2009.14909.x
- Möller, P., Sierk, A. J., Ichikawa, T., & Sagawa, H., 2016, *Atomic Data and Nuclear Data Tables*, 109, 1, doi:10.1016/j.adt.2015.10.002
- Montes, F., Beers, T. C., Cowan, J., et al., 2007, *ApJ*, 671, 1685, doi:10.1086/523084
- Mumpower, M. R., Surman, R., McLaughlin, G. C., & Arahamian, A., 2016, *Progress in Particle and Nuclear Physics*, 86, 86, doi:10.1016/j.ppnp.2015.09.001
- Oda, T., Hino, M., Muto, K., Takahara, M., & Sato, K., 1994, *Atomic Data and Nuclear Data Tables*, 56, 231, doi:10.1006/adnd.1994.1007
- Oechslin, R. & Janka, H.-T., 2006, *MNRAS*, 368, 1489, doi:10.1111/j.1365-2966.2006.10238.x
- Panov, I. V., Korneev, I. Y., Rauscher, T., et al., 2010, *A&A*, 513, A61, doi:10.1051/0004-6361/200911967
- Papaloizou, J. C. B. & Pringle, J. E., 1984, *MNRAS*, 208, 721, doi:10.1093/mnras/208.4.721
- Paschalidis, V., 2016, preprint, arXiv:astro-ph.HE/1611.01519
- Paschalidis, V., Etienne, Z. B., & Shapiro, S. L., 2012, *PRD*, 86, 064032, doi:10.1103/PhysRevD.86.064032
- Perego, A., Rosswog, S., Cabezón, R. M., et al., 2014, *MNRAS*, 443, 3134, doi:10.1093/mnras/stu1352
- Pons, J. A., Reddy, S., Prakash, M., Lattimer, J. M., & Miralles, J. A., 1999, *ApJ*, 513, 780, doi:10.1086/306889
- Qian, Y.-Z. & Woosley, S. E., 1996, *ApJ*, 471, 331, doi:10.1086/177973
- Radice, D., Galeazzi, F., Lippuner, J., et al., 2016, *MNRAS*, 460, 3255, doi:10.1093/mnras/stw1227
- Richers, S., Kasen, D., O'Connor, E., Fernandez, R., & Ott, C. D., 2015, *ApJ*, 813, 38, doi:10.1088/0004-637X/813/1/38
- Roberts, L. F., Kasen, D., Lee, W. H., & Ramirez-Ruiz, E., 2011, *ApJL*, 736, L21, doi:10.1088/2041-8205/736/1/L21
- Roberts, L. F., Lippuner, J., Duez, M. D., et al., 2017, *MNRAS*, 464, 3907, doi:10.1093/mnras/stw2622
- Roberts, L. F., Woosley, S. E., & Hoffman, R. D., 2010, *ApJ*, 722, 954, doi:10.1088/0004-637X/722/1/954
- Roederer, I. U., Lawler, J. E., Sobeck, J. S., et al., 2012, *ApJS*, 203, 27, doi:10.1088/0067-0049/203/2/27
- Rosswog, S., 2015, *International Journal of Modern Physics D*, 24, 1530012-52, doi:10.1142/S0218271815300128
- Rosswog, S., Korobkin, O., Arcones, A., Thielemann, F.-K., & Piran, T., 2014, *MNRAS*, 439, 744, doi:10.1093/mnras/stt2502
- Ruffert, M., Janka, H.-T., & Schaefer, G., 1996, *A&A*, 311, 532, astro-ph/9509006
- Ruffert, M., Janka, H.-T., Takahashi, K., & Schaefer, G., 1997, *A&A*, 319, 122, astro-ph/9606181
- Sekiguchi, Y., Kiuchi, K., Kyutoku, K., & Shibata, M., 2015, *PRD*, 91, 064059, doi:10.1103/PhysRevD.91.064059
- Shakura, N. I. & Sunyaev, R. A., 1973, *A&A*, 24, 337
- Shibagaki, S., Kajino, T., Mathews, G. J., et al., 2016, *ApJ*, 816, 79, doi:10.3847/0004-637X/816/2/79
- Snedden, C., Cowan, J. J., & Gallino, R., 2008, *Annu. Rev. Astron. Astrophys.*, 46, 241, doi:10.1146/annurev.astro.46.060407.145207
- Surman, R., McLaughlin, G. C., Ruffert, M., Janka, H.-T., & Hix, W. R., 2008, *ApJL*, 679, L117, doi:10.1086/589507
- Tanaka, M., 2016, *Advances in Astronomy*, 2016, 634197, doi:10.1155/2016/6341974
- Tanaka, M. & Hotokezaka, K., 2013, *ApJ*, 775, 113, doi:10.1088/0004-637X/775/2/113
- Vlasov, A. D., Metzger, B. D., Lippuner, J., Roberts, L. F., & Thompson, T. A., 2017, preprint, arXiv:1701.03123, arXiv:astro-ph.HE/1701.03123
- Wahl, A. C., 2002, Tech. Rep. LA-13928, Los Alamos National Laboratory, Los Alamos, NM, doi:10.2172/809946
- Wanajo, S., 2013, *ApJL*, 770, L22, doi:10.1088/2041-8205/770/2/L22
- Wanajo, S. & Janka, H.-T., 2012, *ApJ*, 746, 180, doi:10.1088/0004-637X/746/2/180
- Wanajo, S., Sekiguchi, Y., Nishimura, N., et al., 2014, *ApJL*, 789, L39, doi:10.1088/2041-8205/789/2/L39
- Wasserburg, G. J., Busso, M., & Gallino, R., 1996, *ApJL*, 466, L109, doi:10.1086/310177
- Westin, J., Sneden, C., Gustafsson, B., & Cowan, J. J., 2000, *ApJ*, 530, 783, doi:10.1086/308407
- Wu, M.-R., Fernández, R., Martínez-Pinedo, G., & Metzger, B. D., 2016, *MNRAS*, 463, 2323, doi:10.1093/mnras/stw2156